

Detecting galaxy – 21-cm cross-correlation during reionization

Samuel Gagnon-Hartman^{*1}, James Davies¹, and Andrei Mesinger^{1,2}

¹ Scuola Normale Superiore di Pisa, Piazza dei Cavalieri 7, 56126 Pisa, Italy

² Centro Nazionale “High Performance Computing, Big Data and Quantum Computing”

Received September 27, 2023; accepted September 26, 2023

ABSTRACT

The cosmic 21-cm signal promises to revolutionize studies of the Epoch of Reionization (EoR). Radio interferometers are aiming for a preliminary, low signal-to-noise (S/N) detection of the 21-cm power spectrum. Cross-correlating 21-cm with galaxies will be especially useful in these efforts, providing both a sanity check for initial 21-cm detection claims and potentially increasing the S/N due to uncorrelated residual systematics. Here we self-consistently simulate large-scale (1 Gpc³) galaxy and 21-cm fields, computing their cross-power spectra for various choices of instruments as well as survey properties. We use 1080h observations with SKA-low AA* and HERA-350 as our benchmark 21-cm observations. We create mock Lyman alpha narrow-band, slitless and slit spectroscopic surveys, using benchmarks from instruments such as Subaru HyperSupremeCam, Roman grism, VLT MOONS, ELT MOSAIC, and JWST NIRCcam. We forecast the resulting S/N of the galaxy–21-cm cross-power spectrum, varying the galaxy survey area, depth and level of 21-cm foreground contamination for each pair of instruments. We find that the highest S/N is achievable through slitless, wide-area spectroscopic surveys, with the proposed Roman HLS survey resulting in a $\sim 55\sigma$ ($\sim 13\sigma$) detection of the cross power with 21-cm as observed with SKA-low AA* (HERA-350), for our fiducial model and assuming ~ 500 sq. deg. of overlap. Narrow-band dropout surveys are unlikely to result in a detectable cross-power, due to their poor redshift localization. Slit spectroscopy can provide a high S/N detection of the cross power for SKA-low AA* observations. Specifically, the planned MOONRISE survey with MOONS on the VLT can result in a $\sim 3\sigma$ detection, while a survey of comparable observing time using MOSAIC on the ELT can result in a $\sim 4\sigma$ detection. Our results can be used to guide survey strategies, facilitating the detection of the galaxy–21-cm cross-power spectrum.

Key words. 21-cm signal – high-z galaxies

1. Introduction

The 21-cm signal from neutral hydrogen is arguably the most promising probe of the Cosmic Dawn (CD) and the Epoch of Reionization (EoR): two of the last remaining frontiers in modern cosmology. It holds imprints of the physics of the first galaxies (e.g. Mirocha & Furlanetto 2019; Park et al. 2019), the nature of dark matter (e.g. Clark et al. 2018; Villanueva-Domingo 2021; Facchinetti et al. 2024), and perhaps even the role of dark energy (e.g. Adi et al. 2024) during this crucial period of the Universe’s development.

A number of challenges riddle the path towards a measurement of the 21-cm power spectrum. For starters, the interferometer arrays used in tomographic experiments introduce numerous systematic effects into their measurements, all of which must be carefully characterized and accounted for (e.g. Kern et al. 2020; Rath et al. 2024). Furthermore, the highly-redshifted 21-cm signal occupies the same radio band as galactic synchrotron radiation, which overwhelms the cosmic signal by several orders of magnitude. There is also terrestrial contamination to contend with, including radio-frequency interference and the Earth’s ionosphere (e.g. Liu & Shaw 2020).

Owing to these challenges, any claim of a detection of the 21-cm power spectrum will require some form of confirmation in order to gain the trust of the scientific community. The most effective method to bolster confidence in a cosmic 21-cm detection is to correlate it with a signal of known cosmic origin.

In addition to building confidence, a cross-correlation signal could even increase the signal to noise (S/N) of a detection, since the foregrounds of the two signals are unlikely to be correlated. Indeed, several low-redshift studies have confirmed measurements of the 21-cm signal via cross-correlation with galaxy/QSO surveys spanning the same volume (e.g., the Green Bank Telescope Masui et al. 2013; Parkes Radio Telescope Anderson et al. 2018; MeerKAT Cunnington et al. 2023; CHIME CHIME Collaboration et al. 2023a,b). Depending on its nature, the cross-power spectrum could also probe the interaction between galaxies and the intergalactic medium (IGM), yielding complementary information to the auto-power spectra (e.g. Hutter et al. 2023; Moriwaki et al. 2024).

For the EoR / CD 21-cm signal at $z \gtrsim 5$, there are three main candidates for cross-correlation: cosmic backgrounds, intensity maps, and galaxy surveys, each with its own benefits and challenges. The cosmic microwave background (CMB) is a very well established signal, and can cross correlate with the 21-cm signal through secondary anisotropies such as the kinetic Sunyaev-Zel’dovich effect (e.g. Reichardt et al. 2021; Adachi et al. 2022). However, it is an integral (2D) signal and the lack of line-of-sight modes causes them to correlate only weakly with the cosmic 21-cm signal (e.g. Lidz et al. 2009; Mao 2014; Ma et al. 2018; Vrbancic et al. 2020; La Plante et al. 2022). On the other hand, line intensity maps (LIMs) of other emission lines should correlate very strongly with the cosmic 21-cm signal. However most LIMs target metals in the interstellar medium, such as CO and CII, whose corresponding luminosities and achievable S/N of the

* email:samuel.gagnonhartman@sns.it

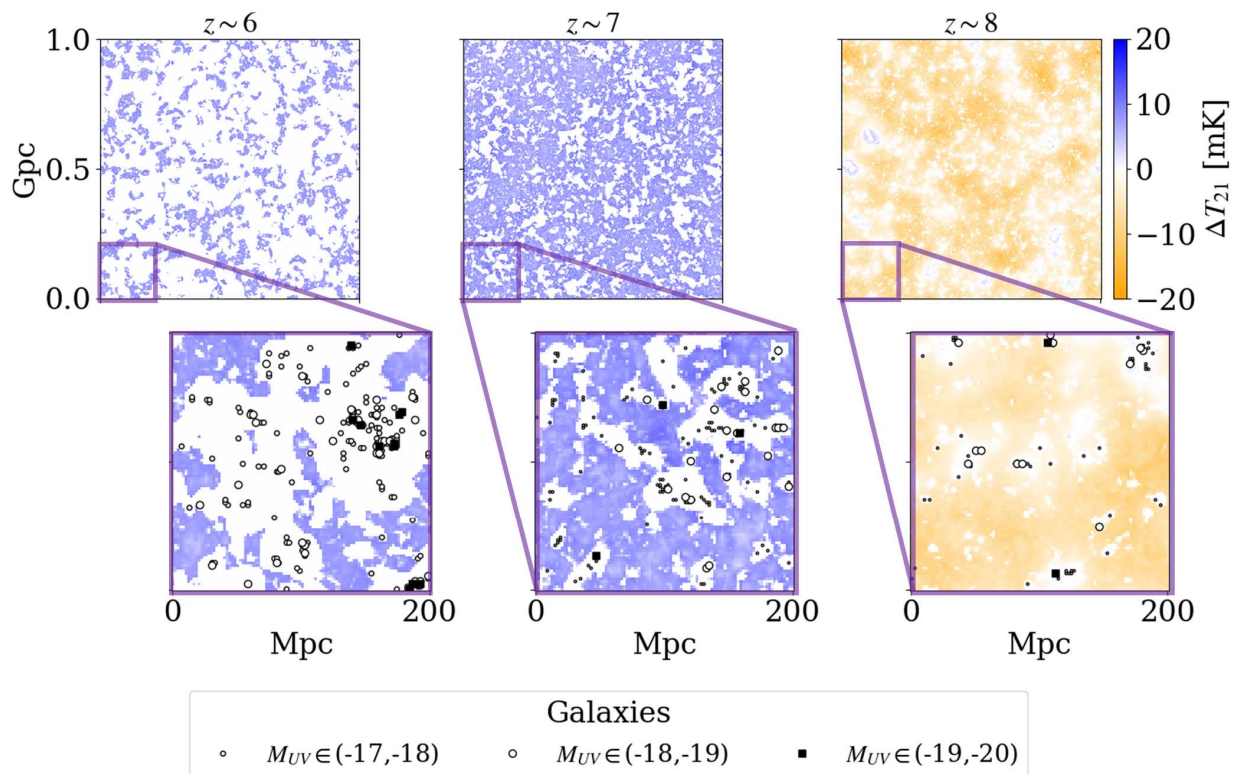


Fig. 1. An example 21-cm brightness temperature field at shown at redshifts 6, 7, and 8 (left to right) with galaxies overlaid on zoomed insets (black). Detectable galaxies at these redshifts preferentially reside in ionized regions, with the brightest, most biased galaxies residing in the largest ionized bubbles. The top row shows slices of the full gigaparsec volume used in this study, while the bottom row zooms into a 200 Mpc corner for clarity. Both the brightness temperature and galaxy fields were generated simultaneously using 21cmFASTv4.

cross correlation with 21-cm are very uncertain at $z \gtrsim 5$ (e.g. Crites et al. 2014; Cooray et al. 2016; Kovetz et al. 2017; Parshley et al. 2018; Heneka & Cooray 2021; Moriwaki & Yoshida 2021; Yang et al. 2022; Pallottini & Ferrara 2023; Fronenberg & Liu 2024).

While LIM experiments will take time to mature, the galaxy mapping toolkit is not only well-established but booming at the time of writing. A plethora of ground and space instruments (e.g. the James Webb Space Telescope, the Subaru Telescope, the Atacama Large Millimeter Array) are currently detecting galaxies deep in the EoR. Spectroscopic galaxy maps, while time-consuming to produce, probe the line-of-sight modes crucial for cross-correlation with the cosmic 21-cm signal while avoiding the challenges associated with LIM (Sobacchi et al. 2016; Hutter et al. 2017; Kubota et al. 2020; Vrbanec et al. 2020; La Plante et al. 2023). As the drivers of reionization, galaxies tightly correlate with ionized bubbles (c.f. Figure 1). Given a sufficient number of galaxies, we should thus detect a strong (anti) correlation with the 21-cm-emitting neutral IGM during the EoR.

In this paper, we quantify the detectability of the cross power spectrum between the 21-cm signal and a galaxy survey spanning the same volume. We self-consistently simulate large-scale (1 Gpc) maps of the 21-cm brightness temperature and the underlying galaxy field. Using empirical relations that include scatter, we make mock observations of galaxy maps with selection based on Lyman alpha and other nebular lines. We quantify the S/N of the galaxy–21-cm cross-power as a function of the galaxy survey’s depth, angular extent, and spectral resolution, as well as the level of foreground contamination of the cosmic 21-cm signal. Based on these estimates, we forecast the S/N for current and upcoming telescopes, including HERA and SKA for 21-cm, and

Subaru, Roman, MOONS and MOSAIC for galaxy maps. We conclude with specific recommendations for surveys seeking to maximize the chance of detecting the galaxy–21-cm cross-power spectrum.

The paper is organized as follows. In Section 2 we present our cosmological simulations. In Section 3 we discuss how we convert our simulation outputs into a mock signal, which involves various assumptions about instrumental effects and sources of systematic uncertainty. In Section 4 we discuss fiducial instruments and survey choices we vary to quantify the detectability of the cross-power spectrum. We present our results in Section 5. We conclude in Section 6 with specific recommendations for surveys seeking to detect the cross power. Throughout we assume a standard Λ CDM cosmology with parameters consistent with the latest *Planck* estimates, wherein $H_0 = 67.66$ km s⁻¹ Mpc⁻¹, $\Omega_m = 0.30966$, $\Omega_b = 0.04897$, $\Omega_k = 0.0$, $\Omega_\Lambda = 0.68846$, and $\sigma_8 = 0.8102$. Unless stated otherwise, all lengths are quoted in comoving units.

2. Simulating the cosmic signal

The cosmic signal in this study refers to two fields: the 21-cm brightness temperature and an overlapping galaxy map. To simulate both fields, we use the latest version of the the public code 21cmFAST (Mesinger & Furlanetto 2007; Mesinger et al. 2011). We then postprocess the cosmic signals, adding telescope noise, removing foreground contaminated regions, and implementing selection criteria for galaxy surveys. This section is split into two subsections, the first of which summarizes how the latest version of 21cmFAST computes cosmological fields and the second

of which discusses our procedure for applying the appropriate observational selection criterion to our simulated galaxy maps.

2.1. Cosmological simulations

Here we use the latest public release, 21cmFASTv4¹ (Davies in prep.) which allows for greater flexibility in characterizing high redshift galaxies. We describe the simulation below, focusing on the new galaxy source model. For further information please consult Davies (in prep.).

21cmFAST creates a 3D realization of the matter field at $z = 30$, evolving it to lower redshifts through second-order Lagrangian Perturbation Theory (2LPT). Here we use simulation boxes that are 1 Gpc on a side, with initial conditions sampled on a 1100^3 grid, which is subsequently down-sampled to a cell size of 2 Mpc. In the previous default version of 21cmFAST, the source fields driving heating and ionization were calculated on filtered versions of the evolved density grid according to the excursion set algorithm (Mesinger et al. 2011). Thus in the default settings, galaxies are not localized on the Eulerian grid. While 21cmFAST has the option to use a discrete halo field via a Lagrangian halo finder named DexM, this algorithm samples over scales with a minimum mass set using the size of the grid cell, rendering it prohibitively slow for halos of mass $M_h \leq 10^{10} M_\odot$ (Mesinger & Furlanetto 2007).

The new model of Davies (in prep.) uses a combination of Lagrangian halo finding and coarse-timestep merger trees to rapidly build 3D realizations of dark matter halos throughout the EoR/CD. These halos are then populated by galaxies whose properties are sampled from empirical relations conditional on their halo mass and other properties. As such, 21cmFASTv4 explicitly accounts for stochastic galaxy formation and generates 3D lightcones of galaxy properties (e.g. stellar mass and star formation rate) alongside the corresponding IGM lightcones. Furthermore, these halos are tracked self-consistently across cosmic time.

We assign a stellar mass and star formation rate to each galaxy by sampling from a log-normal distribution conditioned on the mass of the host halo:

$$\log_{10} M_* \sim \mathcal{N}(\log_{10} \mu_*(M_h), \sigma_*), \quad (1)$$

where σ_* is a redshift-independent free parameter of the model and the mean, so-called stellar to halo mass relation (SHMR), is given by:

$$\mu_* = f_{*,10} \left(\frac{(M_{p1}/M_{p2})^{\alpha_*}}{(M_h/M_{p2})^{-\alpha_*} + (M_h/M_{p2})^{-\alpha_{*2}}} \right) M_h \exp\left(-\frac{M_{\text{turn}}}{M_h}\right) \frac{\Omega_b}{\Omega_m}. \quad (2)$$

Here Ω_b/Ω_m is the mean baryon fraction and the fraction of galactic gas in stars is modeled as a double power law defined by pivot masses (M_{p1} , M_{p2}) and slopes (α_* , α_{*2}) (e.g. Mirocha et al. 2017). Most 21-cm simulations neglect the high-mass turnover in the stellar-to-halo mass relation as these galaxies have a negligible contribution to the total emissivity (e.g. Bouwens et al. 2015; Park et al. 2019; Gillet et al. 2020; Qin et al. 2024). However, these rare, massive galaxies are the ones bright enough to be observed at high redshifts and so are fundamental to our study.

The star formation rate (SFR) of a galaxy is similarly sampled from a log-normal distribution conditioned on the galaxy's stellar mass:

$$\log_{10} \dot{M}_* \sim \mathcal{N}(\log_{10} \mu_{\text{SFR}}(M_h), \sigma_{\text{SFR}}), \quad (3)$$

¹ <https://github.com/21cmFAST/21cmFAST/tree/v4-prep>

with the mean (typically referred to as the star forming main sequence; SFMS):

$$\mu_{\text{SFR}} = \frac{M_*}{t_* H^{-1}(z)}. \quad (4)$$

Here t_* is a free parameter denoting a characteristic star formation timescale in units of the Hubble time $H(z)^{-1}$. Following Davies (in prep.), we decrease the dispersion around the SFMS with increasing stellar mass:

$$\sigma_{\text{SFR}} = \max \left[\sigma_{\text{SFR,lim}}, \sigma_{\text{SFR,idx}} \left(\frac{M_*}{10^{10} M_\odot} + \sigma_{\text{SFR,lim}} \right) \right], \quad (5)$$

These fiducial choices are motivated by results from hydrodynamic simulations (e.g. FirstLight Ceverino et al. 2018, ASTRID Bird et al. 2022; Davies et al. 2023, SERRA Pallottini & Ferrara 2023).

The non-ionizing UV luminosity, sourced primarily by massive, young stars, is taken to be directly proportional to the star formation rate:

$$\dot{M}_*(M_h, z) = \kappa_{\text{UV}} \times L_{\text{UV}}, \quad (6)$$

where we assume the conversion factor $\kappa_{\text{UV}} = 1.15 \times 10^{-28} M_\odot \text{ yr}^{-1} / \text{erg s}^{-1} \text{ Hz}^{-1}$ (e.g. Sun & Furlanetto 2016). Throughout this work, we refer to UV luminosities in units of AB magnitudes, which we compute via the standard relation (e.g. Oke & Gunn 1983):

$$\log_{10} \left(\frac{L_{\text{UV}}}{\text{erg s}^{-1} \text{ Hz}^{-1}} \right) = 0.4 \times (51.63 - M_{\text{UV}}). \quad (7)$$

The fraction of ionizing radiation which escapes the galaxy is characterized by the escape fraction, f_{esc} , whose value is notoriously elusive. Hydrodynamic simulations (e.g., Kimm et al. 2015; Xu et al. 2017; Barrow et al. 2017; Kostyuk et al. 2023), direct observations of low-redshift galaxies (e.g., Izotov et al. 2016; Grazian et al. 2017; Steidel et al. 2018; Pahl et al. 2023), as well as inference from EoR observations (e.g. Nikolić et al. 2023; Qin et al. 2024; Chakraborty & Choudhury 2024) result in very different estimates of f_{esc} and its dependence on galaxy properties. To avoid introducing unmotivated complexity into our model, we adopt the best-fit value of the population-averaged escape fraction, $f_{\text{esc}} = 0.05$, from Nikolić et al. (2023).

Finally, the heating of the IGM before reionization is governed by X-ray emission from the first galaxies. It is likely that the X-ray luminosities from the first galaxies are dominated by high mass X-ray binary stars (HMXBs; e.g. Fragos et al. 2013; Pacucci et al. 2014). The X-ray luminosities of the HMXB population depends on the galaxy's star formation rate and metallicity. We thus sample the X-ray luminosities of the galaxy population from another log-normal distribution whose mean L_X/SFR is a double power-law dependent on SFR and stellar mass, via a gas-phase metallicity Z :

$$\mu_X = \frac{\text{SFR}}{M_\odot \text{ yr}^{-1}} \times L_{X,\text{norm}} \left(\left(\frac{Z}{0.05 Z_\odot} \right)^{0.64} + 1 \right)^{-1} \quad (8)$$

where the fiducial choices are motivated by local HMXB luminosity functions (e.g. Lehmer et al. 2019). We compute the metallicity using the redshift-adjusted fundamental mass metallicity relation (FMZR) from Curti et al. (2020):

$$\frac{Z}{Z_\odot} = 1.23 \left(1 + \left(\frac{M_*}{M_\odot} \right)^{-2.1} \right)^{-0.148} 10^{-0.056z + 0.064}, \quad (9)$$

where

$$M_0 = 10^{10.11} \left(\frac{\text{SFR}}{M_\odot \text{yr}^{-1}} \right)^{0.56}. \quad (10)$$

This flexible galaxy model is anchored to well-established empirical relations (e.g. SHMR, SFMS, FMZR). The free parameters of these relations, including the means and scatters, can eventually be inferred from observations. However, since in this work we provide forecasts for upcoming surveys, we chose "fiducial" values motivated by a combination of observations and hydrodynamic simulations. Table 1 summarizes the fiducial values for all free parameters; for further motivation of these fiducial choices, please see Nikolić et al. (2024) and Davies (in prep.).

With the above galaxy model defining UV and X-ray emissivities, 21cmFAST computes the associated inhomogeneous cosmic radiation fields, tracking the evolution of the temperature and ionization state in each simulation cell (for more details see Mesinger & Furlanetto 2007; Mesinger et al. 2011; Davies in prep.).

The 21-cm brightness temperature of each cell can then be computed as (e.g. Furlanetto et al. 2004):

$$\delta T_b \approx 27 \text{mK} \left(\frac{\Omega_{b,0} h^2}{0.023} \right) \left(\frac{0.15}{\Omega_{m,0} h^2} \frac{1+z}{10} \right)^{1/2} \times x_{\text{HI}} \Delta \left(1 - \frac{T_R}{T_S} \right) \left(\frac{H}{\partial_r v_r} \right), \quad (11)$$

where x_{HI} is the neutral hydrogen fraction, $\Delta \equiv \rho/\bar{\rho}$ is the overdensity, T_R is the CMB temperature, T_S is the spin temperature, and $\partial_r v_r$ is line-of-sight gradient of the velocity of the gas.

The upper row of Figure 1 shows 2D slices through the 21-cm brightness temperature field in our fiducial model at redshifts 6, 7, and 8. We also show a 200 Mpc on a side zoom-in in the bottom row, together with the corresponding galaxy field. The $M_{\text{UV}} < -17$ galaxies shown in the bottom row reside in ionized regions with \sim zero 21-cm emission/absorption. Our fiducial parameter choices result in a midpoint (end) of reionization at $z = 7.7$ (5.5), consistent with the latest observational estimates (e.g. Qin et al. 2024). The IGM is heated by HMXBs to temperatures above the CMB at $z \approx 20$. This milestone roughly marks the regime when the galaxy–21-cm cross power changes sign (e.g. Heneka & Mesinger 2020; Hutter et al. 2023; Moriwaki et al. 2024).

2.2. Galaxy selection based on nebular lines

21cmFASTv4 produces a catalog of galaxies sourcing cosmic radiation fields, which we then need to post-process with observational selection criteria. Every mock survey considered in this study requires its own galaxy map, biased by the corresponding selection criteria and instrument sensitivity.

Unfortunately, selection through broadband photometry results in redshift uncertainties that are too large to estimate a cross power spectrum with 21-cm (e.g. Lidz et al. 2009; La Plante et al. 2023). We therefore base our selection criteria on nebular emission lines. These can be used for narrow-band dropout surveys (e.g. Lyman alpha emitters), low-resolution image spectroscopy (e.g. grism/prism), and high-resolution slit-spectroscopy (requiring follow-up of a photometric candidate sample). We quantify each of these scenarios below.

We consider two fiducial selection criteria: one targeting Lyman- α , and another which selects galaxies on the basis of

H α /H β and [OIII] emission. While Lyman- α is generally intrinsically brighter than other nebular lines, it is more sensitive to ISM/CGM/IGM absorption. Therefore the observed Ly α luminosities have a large sightline-to-sightline variability.

Below we discuss our emission line models. These have been shown to reproduce various observables, including rest-frame UV and Lyman alpha luminosity functions as well as Lyman alpha equivalent width distributions (e.g. Kennicutt 1998; Ly et al. 2007; Gong et al. 2017; Mason et al. 2018; Mirocha et al. 2017; Park et al. 2019).

2.2.1. Lyman alpha

We relate the emergent (escaping the galaxy *after* passing through the ISM and CGM) Lyman alpha luminosity to the galaxy's UV magnitude (c.f. Equation 7) following Mason et al. (2018). The rest-frame, emergent Ly- α equivalent width (EW) is defined as:

$$W = \frac{1216 \text{\AA}}{2.47 \cdot 10^{15} \text{Hz}} \left(\frac{1500}{1216} \right)^{\beta+2} 10^{0.4(M_{\text{UV}}-51.6)} L_{\text{Ly}\alpha}^{\text{emerg}} \quad (12)$$

where $L_{\text{Ly}\alpha}^{\text{emerg}}$ is the emergent luminosity of the Ly- α line and β is the slope of UV continuum emission which we take to be

$$\beta = -2.05 \pm 0.16 - (0.2 \pm 0.07) \times (M_{\text{UV}} + 19.5) \quad (13)$$

following Bouwens et al. (2014). The probability of a galaxy having a nonzero emergent Ly- α emission is

$$A(M_{\text{UV}}) = 0.65 + 0.1 \tanh [3(M_{\text{UV}} + 20.75)]. \quad (14)$$

and the EWs of Ly- α emitters follows the distribution

$$P(W) \propto \exp \left[-\frac{W}{W_c(M_{\text{UV}})} \right], \quad (15)$$

where W_c is the characteristic Ly- α equivalent width, itself a function of M_{UV} :

$$W_c(M_{\text{UV}}) = 31 + 12 \tanh [4(M_{\text{UV}} + 20.25)]. \quad (16)$$

In mapping from M_{UV} to $L_{\text{Ly}\alpha}^{\text{emerg}}$, we draw the probability of emission and the equivalent width of each galaxy from the above distributions and then solve for the luminosity via Equation 12. Mason et al. (2018) determined the parameters of Equations 14 and 16 by fitting tanh functions to post-EoR ($5 \lesssim z \lesssim 6$) galaxies from a Large Program using VLT/FORS2 as well as the VANDELs survey (De Barros et al. 2017; Talia et al. 2023).

We assume all flux blueward of the host halo's circular velocity is scattered out of the line of sight by the CGM. To account for IGM attenuation, we multiply $L_{\text{Ly}\alpha}^{\text{emerg}}$ by $\exp\{-\tau_{\text{EoR}}\}$, where $\tau_{\text{EoR}}(\lambda)$ is the cumulative optical depth of cosmic HI patches along the line of sight to the galaxy. We sample τ_{EoR} from a conditional log-normal distribution motivated by Mesinger & Furlanetto (2008) whose parameters depend on the mean IGM neutral fraction and the mass of the halo hosting the galaxy. For greater detail on this method, refer to Appendix A.

When determining whether or not a particular galaxy is detected in Lyman alpha, we compare the observed flux (i.e. emergent flux attenuated by the IGM) with the flux limit of the instrument of interest. For example, a follow-up of a $M_{\text{UV}} \leq -20$ photometric candidate at $z = 6$, using a spectrograph with a 5σ AB magnitude limit of $m_{\text{AB}}^\alpha \leq 26$ targeting Lyman alpha can only detect Ly- α if the observed equivalent width is greater than $\geq 8 \text{\AA}$.

Figure 2 shows UV luminosity functions (LFs) of our fiducial model at $z = 6, 7,$ and 8 (left to right). The simulated LFs agree with observational estimates (we show in the figure some examples from Finkelstein et al. 2015; Bouwens et al. 2021; Gillet et al. 2020). In Figure 3 we also show the corresponding Lyman alpha LFs at $z \sim 6.6$, together with narrow-band selected Lyman alpha emitter (LAE) LFs from the Subaru telescope (Umeda et al. 2024). Our fiducial model agrees with the observational estimates reasonably well (within 2σ), despite the fact that it uses empirical relations from photometrically-selected galaxies. There is some evidence that our LFs are lower than the LAE ones at the bright end; if this were confirmed, it would make our fiducial estimates of the cross-power spectrum based on Lyman alpha conservatively low.

2.2.2. Selection with other lines

We also consider spectroscopic confirmation targeting other nebular lines. We use as a template the planned JWST survey: the First Reionization Epoch Spectroscopically Complete Observations (FRESCO; Oesch et al. 2023). FRESCO will target a 62 square arcminute field at a depth of $m_{AB} \sim 28.2$ using the NIR-Cam/grism instrument. NIRCam filters are sensitive to $H\alpha$ below redshift 7, and sensitive to [OIII] and $H\beta$ for $z \in (7, 9)$.

We produce separate galaxy maps using the above line selection criterion for various magnitude cutoffs in order to forecast prospects for 21-cm cross-correlation with FRESCO or a FRESCO-like field. We make the common assumption that the luminosity of these low opacity nebular lines traces the star formation rate of the galaxy (e.g. Kennicutt 1998; Ly et al. 2007; Gong et al. 2017):

$$L_{H\alpha} = \text{SFR} \times 1.27 \cdot 10^{41} \frac{\text{erg} \cdot \text{yr}}{\text{s} \cdot M_{\odot}}, \quad (17)$$

$$L_{[\text{OIII}]} = \text{SFR} \times 1.32 \cdot 10^{41} \frac{\text{erg} \cdot \text{yr}}{\text{s} \cdot M_{\odot}}, \quad (18)$$

and

$$L_{H\beta} = \text{SFR} \times 7.14 \cdot 10^{40} \frac{\text{erg} \cdot \text{yr}}{\text{s} \cdot M_{\odot}}, \quad (19)$$

where the SFR is in units of M_{\odot}/yr and the luminosity is in erg/s .

3. Computing the S/N of the cross-power spectrum

After computing the cosmic signals, we determine the detectability of the galaxy–21-cm cross-power spectrum given a specific pair of instruments. We compute the power spectrum in cylindrical coordinates $(k_{\perp}, k_{\parallel})$ as this is the natural basis for interferometers seeking to maximize the signal to noise of a detection. Furthermore, this basis relegates foreground contamination to an easily-excised (at least in principle) corner of Fourier space. Here, k_{\perp} refers to wavemodes in the sky plane and k_{\parallel} refers to wavemodes along the line of sight. Thus, a cylindrical cross-power spectrum is constructed by independently averaging Fourier modes along the line of sight and in sky plane bins.

We split each lightcone into redshift chunks, each with a frequency-domain depth of $\Delta\nu = 6$ MHz centered on redshift z . From each chunk we compute the cross-power spectra:

$$P_{21,g}(k_{\perp}, k_{\parallel}, z) = \langle \delta T_b^*(z) \delta_g(z) \rangle_{k_{\perp}, k_{\parallel}}, \quad (20)$$

Table 1. Fiducial galaxy parameters.

Parameter	Description	Value
$f_{*,10}$	SHMR normalisation	0.05
α_*	Power-law index of SHMR	0.5
α_{*2}	High mass power-law index of SHMR	-0.61
M_{p1}	lower pivot mass in SHMR	$10^{10} M_{\odot}$
M_{p2}	upper pivot mass in SHMR	$2.8 \times 10^{11} M_{\odot}$
σ_*	lognormal scatter in SHMR	0.3 dex
C_*	auto-correlation timescale of SHMR	0.5
t_*	SSFR normalisation	0.5
$\sigma_{\text{SFR,lim}}$	minimum lognormal scatter in SSFR	0.19 dex
$\sigma_{\text{SFR,idx}}$	Power-law scaling of SSFR scatter	-0.12
C_{SFR}	auto-correlation timescale of SSFR	0.1
$L_{X,\text{norm}}$	L_X/SFR Normalisation	$10^{40.5} \text{ergs}^{-1}$
σ_X	lognormal scatter in L_X/SFR	0.5 dex
C_X	auto-correlation timescale of L_X/SFR	0.5
$f_{\text{esc},10}$	Escape fraction normalisation	0.1
α_{esc}	Escape fraction power-law scaling	0.5

where $P_{21,g}(z)$ is the galaxy–21-cm cross-power spectrum, $\delta T_b(z)$ is the 21-cm brightness temperature field, and $\delta_g(z) \equiv n_g(z)/\bar{n}_g(z) - 1$ is the galaxy overdensity field.

The averaging in the above equation is computed only over wavemodes that are accessible to a specific instrument/survey, and that are not highly contaminated by foregrounds or systematics. Averaging over systematics-contaminated modes might still improve the S/N, given that uncorrelated systematics do not impact the *mean* of the cross-power, even though they increase the variance (e.g. Fronenberg & Liu (2024)). However, in order to quantify exactly which wavemodes should be excised, we would need to forward-model systematics or foreground residuals. We save this for future work, here making the simplifying assumption that foreground/systematics-dominated wavemodes are unusable while the remaining wavemodes include no residual systematics.

We show a schematic of these contaminated or missing regions in 2D Fourier space in Figure 4. Each shaded region illustrates some range of wavemodes that contribute negligibly to the cross-power due to some properties of the instrument/survey/systematics. These include the area of the overlap between the galaxy field and 21-cm field (limited by the galaxy survey’s footprint), the redshift uncertainty of the galaxies, and contamination by 21-cm foregrounds.

The galaxy survey will typically have the smaller of the two footprints², and it can range from tens – hundreds of square degrees for narrow-band dropout or grism surveys to \lesssim sq. deg for deep follow-up of photometric candidates using high-resolution spectroscopy. The area of the galaxy survey sets the largest on-sky scale (smallest k_{\perp}) accessible for computing the cross-power spectrum. Similarly, the galaxy redshift uncertainty effectively sets the smallest accessible line of sight scale (largest k_{\parallel} ; as described further below, we do not excise the larger k_{\parallel} modes but instead account for the corresponding uncertainty when computing the noise). The redshift uncertainty we consider in this work ranges from $\delta z \sim 0.05$ for narrow-band LAE surveys to $\delta z \sim 0.001$ for spectroscopy³ (c.f. Table 2).

² For example, the “wedding-cake” strategy envisioned for the SKA-low Key Science Project is expected to cover up to $\sim 10^4$ sq. deg., while the HERA observing stripe covers ~ 4000 sq. deg.

³ In principle, the redshift uncertainty is determined by a combination of instrument resolution, peculiar velocity, and the offset of the Lyman alpha line from systemic. The latter two effects set a lower limit for

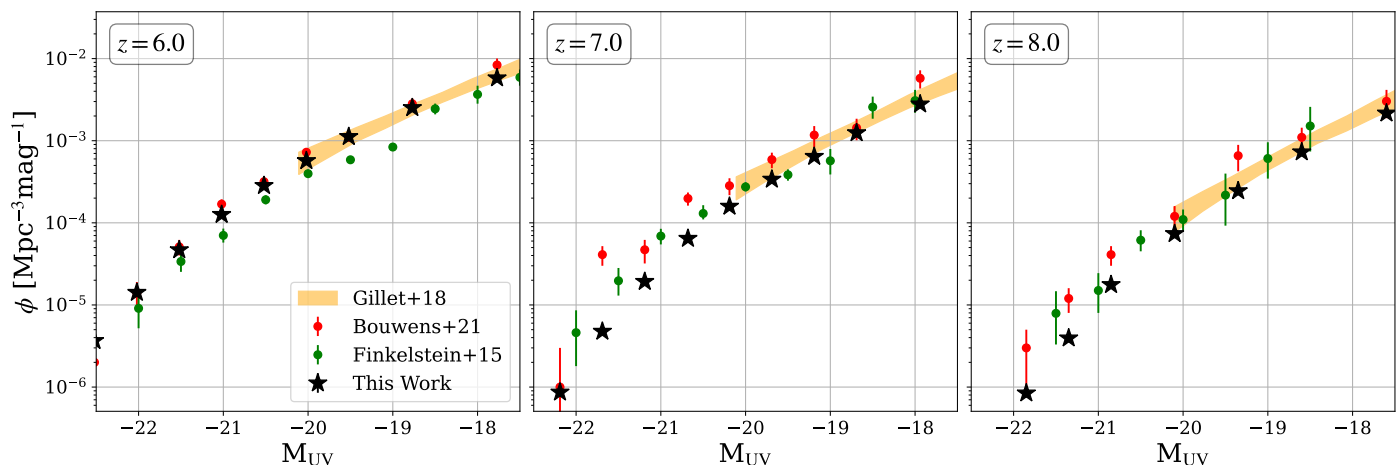


Fig. 2. UV luminosity functions (LFs) at $6 \leq z \leq 8$ from our fiducial model, compared with several observational estimates. We show *Hubble* estimates from Bouwens et al. (2021) and Finkelstein et al. (2015), as well as the observation-averaged posterior from Gillet et al. (2020) (1σ credible interval).

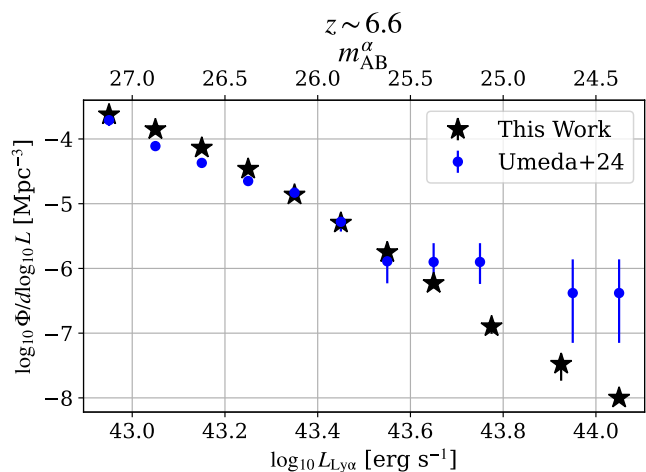


Fig. 3. Lyman alpha luminosity functions at $z \sim 6.6$. Our fiducial model is based on equivalent width distributions of photometrically-selected candidates (see text for details). We show also narrow-band selected LAE LFs from Subaru (Umeda et al. 2024).

Finally, the spectral smoothness of 21-cm foregrounds excludes the lowest k_{\parallel} scales. More importantly, the response function of 21-cm interferometers results in leakage of foreground emission into a wedge-shaped region of Fourier space, overwhelming the cosmic signal (e.g. Datta et al. 2010; Pober et al. 2014; Dillon et al. 2014; Liu et al. 2014a; Pober 2014). To quantify the “wedge” contaminated region, we use different slopes in cylindrical k -space (e.g., Thyagarajan et al. 2015):

$$m(z) \equiv \frac{k_{\parallel}}{k_{\perp}} = \sin(\theta_{\text{FoV}}) \frac{D_c(z)H(z)}{c(1+z)}, \quad (21)$$

where $D_c(z)$ is the comoving distance to that redshift and θ_{FoV} is the angular radius of the field of view of the beam of the 21-cm interferometer (see also Munshi et al. 2025 for an alternate characterization of the wedge). We consider three foreground scenarios in this study: a “fiducial” scenario where only k -modes up

to the achievable redshift uncertainty, which is of order $\delta z \sim 0.001$. We postpone a more careful treatment of each of these terms to future work focusing on specific instruments.

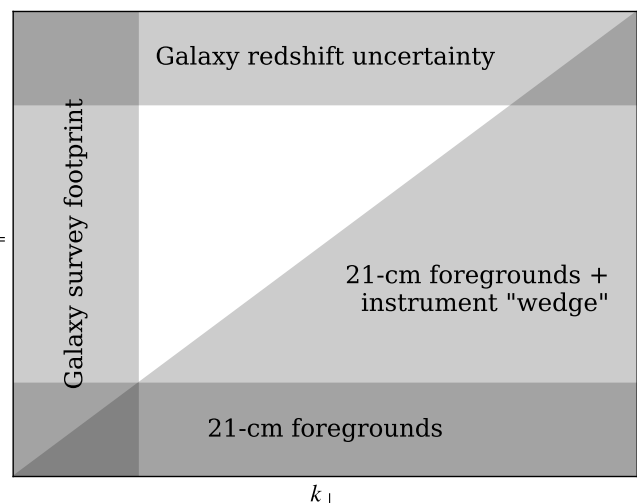


Fig. 4. Schematic illustrating regions in the cylindrical power spectrum which contribute negligibly to the cross-power S/N due to instrument/survey/systematic limitations.

to the slope in Equation 21 are foreground-dominated, a “pessimistic” scenario in which we double the slope, and an “optimistic” scenario where we half the slope to represent the recovery of lost Fourier modes via advanced foreground mitigation techniques (e.g., Hothi et al. 2020; Gagnon-Hartman et al. 2021; Bianco et al. 2024; Kennedy et al. 2024). Foreground scenarios typically vary from horizon-limited to beam-limited, with the former corresponding to our fiducial scenario and the latter analogous to our pessimistic scenario. We also vary the extent of intrinsic foregrounds in each scenario, excising $k_{\parallel} \leq 0.07 \text{ Mpc}^{-1}$ for the fiducial and optimistic scenarios and $k_{\parallel} \leq 0.175 \text{ Mpc}^{-1}$ for the pessimistic one (Kubota et al. 2018).

Having defined the cross-power spectrum as well as the region in cylindrical Fourier space over which it is computed, we move on to estimating the associated uncertainty. The variance of the cross-power spectrum is (c.f. Lidz et al. 2009):

$$\sigma_{21,g}^2(k_{\perp}, k_{\parallel}) = \text{var} \left[\frac{1}{T_0(z)} P_{21,g}(k_{\perp}, k_{\parallel}) \right], \quad (22)$$

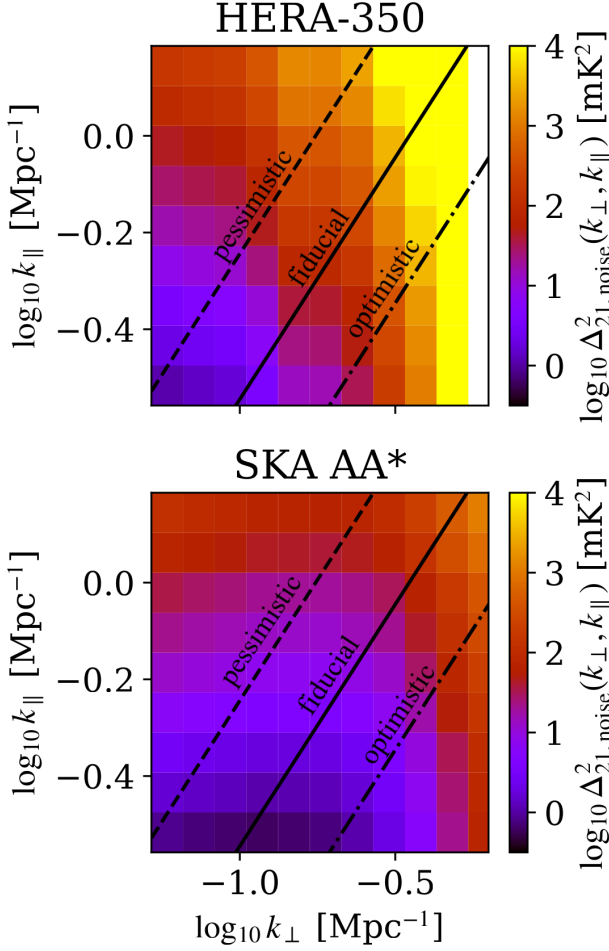


Fig. 5. The cylindrical noise power spectra of HERA-350 (*top*) and SKA-low AA* (*bottom*) for a fiducial 1000 hour observation at redshift 6.1. The diagonal lines in each panel denote the three choices for wedge excision considered in this work.

which reduces to

$$\sigma_{21,g}^2(k_{\perp}, k_{\parallel}) = \frac{1}{2} \left[P_{21,g}^2(k_{\perp}, k_{\parallel}) + \sigma_{21}(k_{\perp}, k_{\parallel}) \sigma_g(k_{\perp}, k_{\parallel}) \right]. \quad (23)$$

Similarly, the variance of the auto power spectra can be written as a sum in quadrature of the cosmic variance and noise power:

$$\sigma_{21}^2(k_{\perp}, k_{\parallel}) = \frac{1}{2} \left[\frac{1}{T_0^2(z)} P_{21}(k_{\perp}, k_{\parallel}) + P_{21}^{\text{noise}}(k_{\perp}, k_{\parallel}) \right]^2 \quad (24)$$

and

$$\sigma_g^2(k_{\perp}, k_{\parallel}) = \frac{1}{2} \left[P_g(k_{\perp}, k_{\parallel}) + P_g^{\text{noise}}(k_{\perp}, k_{\parallel}) \right]^2, \quad (25)$$

where the first terms on the right hand sides correspond to cosmic variance, while P_{21}^{noise} and P_g^{noise} correspond to the 21-cm thermal noise and galaxy redshift uncertainty, respectively. We describe these in turn below.

We compute the 21-cm thermal noise power spectrum, P_{21}^{noise} , using 21cmSense (Poher et al. 2014; Murray et al. 2024). We use antenna layouts corresponding to the full HERA-350 array (Berkhout et al. 2024), as well as the initial AA* deployment of SKA-low (Sridhar 2023). We assume a 1080h total integration of

drift scan for HERA-350/SKA-low with 6 hours of observation per night over 180 days⁴. The resulting thermal noise are plotted in Figure 5. Our mock survey with SKA-low results in overall lower noise. This is most evident at the largest k_{\perp} which are better sampled due to SKA-low’s longer baselines in the core. In the figure we also show with diagonal lines the three different wedge scenarios considered in this work. We see that optimistic foreground removal would benefit SKA-low far more than HERA-350, since these wedge modes in HERA have very high levels of thermal noise. Indeed foreground-avoidance was a design choice for HERA.

We adopt the galaxy noise model of Lidz et al. (2009), wherein the shot noise sets the minimum noise level and redshift uncertainty governs line-of-sight positional uncertainty:

$$P_g^{\text{noise}}(k_{\parallel}) = \frac{1}{n_{\text{gal}}} \exp \left[k_{\parallel}^2 \left(\frac{c\sigma_z}{H(z)} \right)^2 \right], \quad (26)$$

where n_{gal} is the number density of galaxies in the survey volume and σ_z is the redshift uncertainty set by the instrument. This form for $P_g^{\text{noise}}(k_{\parallel})$ states that the galaxy power spectrum is suppressed by a Gaussian kernel whose width equals the characteristic scale of redshift uncertainties in the field (Seo & Eisenstein 2003). Fisher et al. (1993) and Feldman et al. (1994) have shown that this suppression arises naturally in measured galaxy power spectra. As shown in Table 2, we use three fiducial values for σ_z corresponding to narrow-band dropouts (LAE; e.g. Ouchi et al. 2018), imaging (i.e. slitless) spectroscopy (grism/prism; e.g. Wang et al. 2022; Oesch et al. 2023), and slit spectroscopy (e.g. Evans et al. 2015; Maiolino et al. 2020).

The signal-to-noise ratio in each bin (k_{\perp}, k_{\parallel}) depends not only on the cross-power amplitude and uncertainty, but also on the number of Fourier modes sampled by that bin (i.e. sample variance). Assuming that bins are of equal length in log-space, the number of modes per bin is

$$dN(k_{\perp}, k_{\parallel}) = \frac{k_{\perp}^2 k_{\parallel} V_{\text{survey}}}{(2\pi)^2} d \ln k_{\perp} d \ln k_{\parallel}, \quad (27)$$

where V_{survey} is the volume of the survey in comoving units. The signal-to-noise ratio in a single bin adds in quadrature with the number of Fourier modes sampling that bin:

$$\hat{s}(k_{\perp}, k_{\parallel}) = \sqrt{dN(k_{\perp}, k_{\parallel})} \frac{P_{21,g}(k_{\perp}, k_{\parallel})}{\sigma_{21,g}(k_{\perp}, k_{\parallel})}. \quad (28)$$

Following Furlanetto & Lidz (2007), we compute the global signal-to-noise ratio as the sum in quadrature of⁵ the signal-to-noise ratios in each (k_{\perp}, k_{\parallel}) bin and z :

$$S/N^2 = \sum_{k_{\perp}, k_{\parallel}, z} \hat{s}^2(k_{\perp}, k_{\parallel}, z). \quad (29)$$

⁴ The SKA-low AA* beam covers a stripe on the sky with a width of 3.68°. Integrating for 6 hours per night over the same stripe produces a survey footprint of 332 sq. deg.. Similarly, HERA covers a stripe of width 11.0° and thus produces a survey footprint of 990 sq. deg. (Murray et al. 2024). We assume Gaussian beams, and the widths quoted above correspond to the 3σ extents.

⁵ Our choice to treat the global S/N as the quadrature sum of the S/N in each bin reflects our assumption that the noise in each Fourier mode is statistically independent. This assumption results in a modest overestimation of the signal-to-noise ratio (e.g., Liu et al. (2014a), Liu et al. (2014b), Prelogović & Mesinger (2023)).

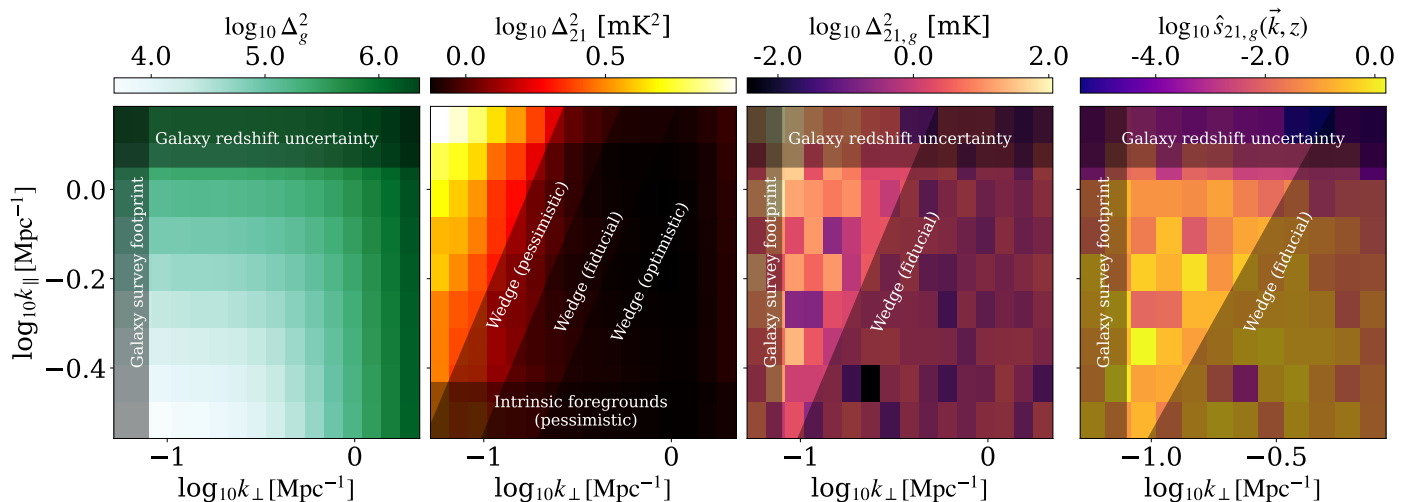


Fig. 6. The power spectra of the galaxy field, 21-cm brightness temperature field, their cross-power spectrum, and the signal-to-noise ratio of the cross-power spectrum as a function of k_{\parallel} and k_{\perp} for a fiducial scenario (left to right). Overlaid are various noise-dominated/excluded regions imposed by systematics and observational effects. The 21-cm brightness temperature power spectrum includes cuts showing the three foreground+instrument (i.e. "wedge") contamination scenarios considered in this study. In this illustrative example, the galaxy survey footprint corresponds to ~ 1 sq. deg. at $z \sim 6$ while the galaxy redshift uncertainty corresponds to $\delta z \sim 0.01$ that is characteristic of slitless spectroscopy.

Figure 6 illustrates the principal data products in our pipeline for estimating the signal-to-noise ratio of the cross-power spectrum. The first two panels from the left show the galaxy and 21-cm auto-power spectra, respectively, as computed from a 1 Gpc coeval cube at $z = 6.1$. The third panel shows the galaxy–21-cm cross-power spectrum of the same cube. Here we see that the correlation between k -modes is weaker than in the galaxy or 21-cm spectra. The rightmost panel shows the resulting signal-to-noise from Equation 28. Superimposed on each panel are shaded regions corresponding to wavemodes inaccessible due to survey/instrument/systematics limitations. The final S/N depends primarily on the unshaded wavemodes in the rightmost panel, extended to include also other redshift bins.

4. Mock observations

The galaxy–21-cm cross-power depends on the telescopes used for each observation as well as the survey strategies. As discussed above, our fiducial 21-cm observations are 1080h total integration with either HERA-350 or SKA-low AA*. For simplicity, we do not vary the 21-cm survey specifications.

We consider three general types of instruments used for galaxy surveys, in order of increasing redshift accuracy⁶:

1. *Narrow-band dropout* - using narrow photometric bands to identify Lyman alpha line emission. Galaxies thus identified are commonly referred to as LAEs, and have an associated redshift uncertainty determined by the photometric bands used in the drop-out selection. Here we take Subaru as a fiducial telescope, assuming a redshift uncertainty of 5% (Ouchi et al. 2018).
2. *Imaging (slitless) spectroscopy* - slitless spectrographs (e.g. grism) provide low-resolution multiple spectra within a contiguous field, without requiring pre-selection of candidates through broad-band photometry. We take *Roman* as our fiducial telescope for LAE-selected surveys and *JWST* (NIR-

⁶ As mentioned above, we do not consider broad-band photometry (i.e. Lyman break galaxy surveys), because the corresponding redshift uncertainties are too large to be useful for cross correlation with 21-cm (e.g. La Plante et al. 2023).

Cam) for $H\alpha/H\beta/OIII$ -selected surveys. We assume a redshift uncertainty of 1% for both instruments (Wang et al. 2022).

3. *Slit spectroscopy* - high resolution spectrographs result in the smallest redshift uncertainty. However, slit spectroscopy requires follow-up of photometric candidates, either from existing fields or new fields. Here we assume that photometric candidates of sufficient depth are available (e.g. Euclid Deep Field South Euclid Collaboration et al. 2024, SILVERRUSH Ouchi et al. 2018, legacy *Hubble* fields), and the bottleneck comes from the spectroscopic follow-up of Lyman alpha. We adopt a slit spectroscopy redshift uncertainty of 0.1% (e.g. Maiolino et al. 2020).

For each pair of galaxy–21-cm instruments, we compute the S/N of the cross power as a function of the galaxy survey area and AB magnitude limit in the relevant observing band: denoted as m_{AB}^{α} for Ly- α -selected surveys and m_{AB} for $H\alpha/OIII$ -selected surveys. Figure 7 illustrates the stochastic relationship between intrinsic galaxy parameters and Ly- α emission, showing that a galaxies' UV continuum magnitude M_{UV} does not uniquely determine its m_{AB}^{α} . Superimposed are horizontal lines corresponding to the Ly- α band limiting AB magnitudes of the MOONRISE and Roman HLS surveys (Maiolino et al. 2020; Wang et al. 2022). Note that slit-spectroscopic galaxy surveys require a photometric candidate survey, complete down to some M_{UV} , on which they perform follow-up observations. We do not investigate the effect of M_{UV} incompleteness of the photometric candidates in this study, assuming that a candidate survey is deep enough for a slit-spectroscopic follow-up survey of a given m_{AB}^{α} limit to be performed with full completeness. For example, a Lyman alpha spectroscopic survey at $z \sim 7$ with a depth of $m_{AB}^{\alpha} \leq 26$ would require follow-up of photometrically-selected candidates down to $M_{UV} \leq -20$ in order to be $\geq 95\%$ complete (c.f. Fig. 7).

We produce six realizations of each observed galaxy field for magnitude cuts ranging from $m_{AB}^{\alpha} = 25$ to $m_{AB}^{\alpha} = 30$ and average the S/N at each magnitude cut. In our calculation of band magnitude, we assume that the relevant band is dominated by line emission, which is reasonable since only LAEs with equivalent

Table 2. 21-cm and galaxy survey parameters considered.

Interferometer	Detection Type	Line Targeted	δz	Footprint Range	Depth Range (m_{AB})	Figure(s)
SKA-low	Narrow-band dropout	Ly- α	$5 \cdot 10^{-2}$	10 – 20 sq. deg.	25.5 – 30	8,9,10
SKA-low	Grism $z > 7.2$	Ly- α	10^{-2}	0 – 25 sq. deg.	25 – 27	8,9,10
SKA-low	Spectroscopy	Ly- α	10^{-3}	0 – 4 sq. deg.	24 – 27	8,9,10
HERA	Narrow-band dropout	Ly- α	$5 \cdot 10^{-2}$	10 – 20 sq. deg.	25.5 – 30	11
HERA	Grism $z > 7.2$	Ly- α	10^{-2}	0 – 120 sq. deg.	25 – 27	11
HERA	Spectroscopy	Ly- α	10^{-3}	0 – 4 sq. deg.	24 – 27	11
SKA-low	Grism	H α /[OIII]	10^{-2}	0 – 350 sq.arcmin.	27 – 30	12

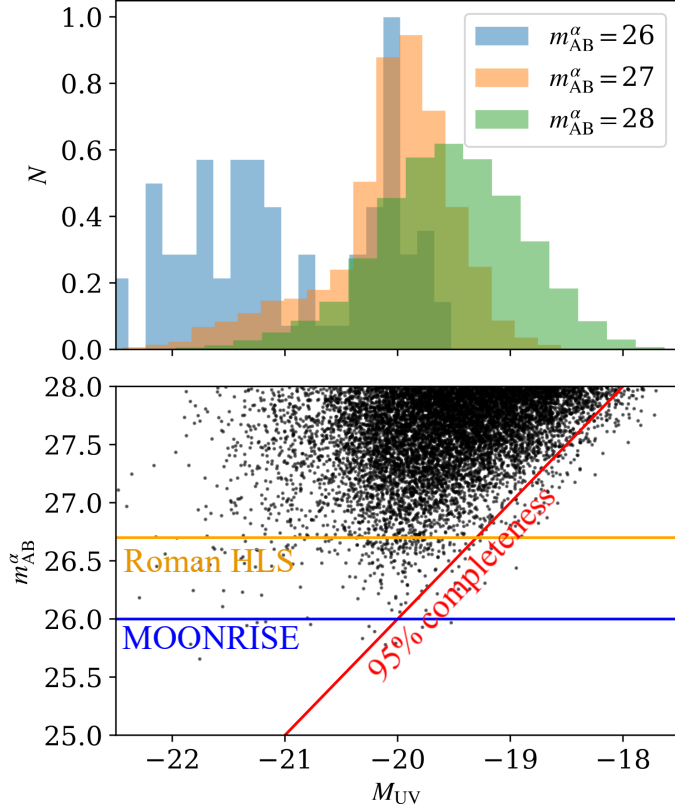


Fig. 7. The distribution of UV continuum magnitudes (M_{UV}) and Lyman- α band AB magnitudes (m_{AB}^{α}) of galaxies from a 1 Gpc on a side coeval cube at $z = 7.2$. The bottom panel includes only 10% of the galaxies in the volume, for clarity. The horizontal lines indicate the limiting magnitudes for Roman HLS and the MOONRISE survey (Maiolino et al. 2020; Wang et al. 2022), while the diagonal line corresponds to the M_{UV} limit required for 95% completeness at a given m_{AB}^{α} . The top panel shows the distributions of M_{UV} for $m_{\text{AB}}^{\alpha} = (26, 27, 28)$ in our model. We compute the 95% completeness criterion by integrating over these distributions.

width greater than unity are detectable at the considered magnitude cuts. We find that the total S/N of the cross-power spectrum varies fairly smoothly between magnitude cuts, so we devise an analytic form for S/N as a function of magnitude cut for each galaxy selection criterion, described in Appendix C. Moreover, the S/N varies trivially with the survey angular area, requiring only a cut in cylindrical Fourier space as well as the noise rescaling introduced in Equation 27. The redshift uncertainty is likewise easy to implement via Equation 26.

4.1. Benchmark galaxy surveys

Although our predictions for cross-spectrum S/N can be used to design new surveys, we use existing/proposed ones as a reference. These are listed in Table 3. Of these, SILVERRUSH is already underway and FRESKO, MOONRISE, and HLS are slated to occur in the coming years. We also consider a prospective spectroscopic follow-up survey using ELT MOSAIC modeled after MOONRISE.

The Systematic Identification of LAEs for Visible Exploration and Reionization Research Using Subaru HSC (SILVERRUSH) survey is a long-running program for the identification of tens of thousands of LAEs via narrow-band dropout covering redshifts 2 – 7 (Ouchi et al. 2018). The survey area of SILVERRUSH ranges from 13.8 square degrees at $z \sim 5.7$ to 21.2 square degrees at $z \sim 6.6$ (Umeda et al. 2024). To split the difference between these survey footprints while producing the same number of galaxies, we take our SILVERRUSH benchmark to cover an equal 16 square degrees across all redshifts and to observe down to $m_{\text{AB}}^{\alpha} = 26$. The limiting factor when computing the S/N of the cross power using SILVERRUSH is its narrow-band dropout strategy, which results in a relatively large redshift uncertainty. However, many of these LAE are being followed up with spectroscopy, which should reduce these errors in the future.

The Nancy Grace Roman Space Telescope will conduct a High Latitude Survey (HLS) over a huge swathe of sky covering ~ 2000 sq. deg. using its near-IR grism. Of this, 500 sq. deg. overlaps with the HERA stripe, and for ease of comparison between cross-correlation forecasts with SKA-low AA* and HERA-350 we limit the effective survey footprint of the Roman HLS to 500 sq. deg.. Using ~ 0.6 years of observing time, the survey is expected to detect tens of thousands of $z > 5$ galaxies via the Lyman break technique. Due to the near-IR band's frequency range, Roman can only detect Lyman- α emission at $z > 7.2$ (Wang et al. 2022). La Plante et al. (2023) forecast the significance of a cross-power spectrum detection made using a Lyman- α survey from Roman and a 21-cm field measured using HERA. Here we confirm their findings, and extend them to an SKA-low AA* measurement of the 21-cm signal. Although HLS benefits from a large sky area, its imaging spectroscopy is limited to $z > 7.2$, which significantly limits the S/N compared to surveys extending to lower redshifts. The LBG sample from Roman could however be followed-up with slit spectroscopy (with, e.g. MOSAIC on the ELT), providing galaxy maps throughout the EoR.

The First Reionization Epoch Spectroscopically Complete Observations (FRESKO) survey is a Cycle 1 medium program slated for execution on the James Webb Space Telescope (Oesch et al. 2023). FRESKO will cover 62 square arcminutes and observe out to a depth of $m_{\text{AB}} \approx 28.2$ using NIRCcam/grism. FRESKO targets H α at $z < 7$ and [OIII] and H β for $z \in (7, 9)$. Although its target area is much smaller than the other bench-

Table 3. Benchmark galaxy surveys considered in this study.

Survey	Depth (m_{AB})	Footprint	δz	Redshift
SILVERRUSH (Subaru/Hyper Suprime-Cam)	26	16 sq. deg.	$5 \cdot 10^{-2}$	$z \sim 6.6$
HLS (Nancy Grace Roman Space Telescope)	26.7	500 sq. deg.	10^{-2}	$z > 7$
FRESCO (James Webb Space Telescope NIRCam grism)	28.2	62 sq. arcmin.	10^{-2}	$z > 6$
MOONRISE (VLT MOONS)	26	1.2 sq. deg.	10^{-3}	$z > 5$
a prospective ELT MOSAIC spectroscopic survey	26 – 28	1–3 sq. deg.	10^{-3}	$z > 5$

mark surveys, FRESCO observes to much deeper magnitudes and selects on low-opacity emission lines which allows for more accurate redshift determination (here for simplicity we use the same redshift uncertainty for all slitless surveys).

The MOONS Redshift-Intensive Survey Experiment (MOONRISE) is a Guaranteed Observing Time program of the MOONS instrument, a powerful spectrometer slated for deployment at the Very Large Telescope (VLT) (Maiolino et al. 2020). MOONRISE will spectroscopically follow up ~ 1100 candidate LAEs down to $m_{AB}^{\alpha} = 26$ in a ~ 1 square degree field at $z > 5$. MOONRISE walks the middle path of reasonable survey area, moderate survey depth, and good redshift uncertainties, making it a promising candidate among slit spectroscopic surveys for cross-correlation with 21-cm.

Finally, we provide forecasts using a prospective survey on the next-generation multiplex spectrograph ELT MOSAIC, currently in development for deployment at the Extremely Large Telescope (ELT). We provide forecasts for MOONRISE-like surveys performed using ELT MOSAIC assuming an $m_{AB}^{\alpha} = 25.3$ 5σ 5-hour limiting magnitude (Evans et al. (2015); C. Kehrig, private communication).

5. Results

Our results are summarized in Figures 8–12. Each figure shows the S/N of the galaxy–21-cm cross-power spectrum as a function of observing depth and survey footprint, for narrow-band dropout, slitless and slit spectroscopy (*left to right panels*). Different figures vary the 21-cm instrument (HERA-350 vs SKA-low AA*) as well as the level of 21-cm wedge contamination (optimistic, fiducial, pessimistic). In the spectroscopy panels for Ly α -selected galaxy surveys we show 100 and 1000 hour isochrones for observations using the ELT MOSAIC instrument. These isochrones correspond to the total observation time, equal to the number of 40 sq. arcmin pointings required to reach the desired survey footprint on the vertical axis, times the exposure time per pointing required for a $\geq 5\sigma$ detection down to the given limiting m_{AB}^{α} on the horizontal axis (using the latest MOS-NIR-LR sensitivity estimates; C. Kehrig, private communication).

Increasing the redshift uncertainty suppresses S/N exponentially, requiring an exponential rise in the number of galaxies detected to compensate. This may be achieved by either dramatically increasing the survey footprint or increasing the observing depth by a few magnitudes. Therefore we evaluate the S/N of narrow band dropout and grism surveys on a larger range of footprint sizes and a deeper range of observing depths than the slit spectroscopic surveys. Furthermore, we limit the sensitivity of the grism surveys in this experiment to $z > 7.2$ to reflect the filter of the Nancy Grace Roman Space Telescope’s grism.

In all cases we see that once surveys are deeper than $m_{AB}^{\alpha} \sim 25$, the S/N increases more readily with survey area than with the observing depth. For spectroscopic surveys, we find that targeting a depth of $m_{AB} \sim 26$ and maximizing the contiguous survey

footprint yields the highest S/N per unit survey time. We discuss this result in greater detail in Appendix C.

5.1. SKA–Lyman Alpha

Figure 8 shows our results for a Lyman- α galaxy survey paired with an SKA-low AA* 21-cm measurement assuming the fiducial foreground scenario. We see in the left panel that the SILVERRUSH sample with no spectroscopic follow-up is insufficient for a cross-power detection. This is contrary to some previous claims (e.g. Sobacchi et al. 2016; Hutter et al. 2018), which had more simplistic treatments of redshift uncertainties in the LAE sample. Indeed, even an extremely deep narrow-band dropout survey (i.e., $m_{AB}^{\alpha} < 30$) of similar area cannot yield a significant cross-spectrum detection, except in the case of optimistic 21-cm foreground recovery, highlighting the importance of small redshift uncertainties in measuring the cross-power spectrum.

The middle panel includes a forecast for Roman HLS using a survey footprint equivalent to the beam size of SKA-low AA*. Due to Roman’s enormous angular survey extent, this is the only case where the footprint for cross-correlation is limited by the field of view of the 21-cm instrument. We find that a single patch of the SKA-low AA* beam within Roman HLS yields an 8σ detection of the cross-power spectrum. Tiling multiple beams can increase the signal to noise. For example, 47 patches of the SKA-low AA* beam can fit within 500 sq. deg. of overlapping area, which would bring the cumulative S/N from to $\sqrt{47} \cdot 8 = 54.8$.

In the right panel, we see that the planned MOONRISE survey should be sufficient to measure the cross-power spectrum at a $\sim 3\sigma$ significance. Furthermore, the dashed contours delineating prospective MOSAIC configurations imply that a similar survey using MOSAIC could achieve a $\sim 4\sigma$ measurement of the cross-power spectrum in ~ 500 hours of observation targeting $\sim 1\text{--}3$ sq. deg. Extending this to 1000h can bring the S/N up to 5σ .

Figures 9 and 10 show our results for the same Lyman- α galaxy survey and SKA-low observations, but assuming pessimistic and optimistic 21-cm foregrounds, respectively. We see in Figure 9 that the significance of a cross-spectrum measurement depends very strongly on the level of the foregrounds, and that our strong foreground case precludes a detection of the cross-power spectrum using the MOONRISE survey. However, a 1000-hour observation using ELT MOSAIC could yield a $\sim 3\sigma$ detection. We find that increasing the number of telescope pointings (assuming equal exposure time per pointing) yields more S/N per unit observing time than boosting exposure depth. Figure 10 shows that even in the scenario where a significant portion of 21-cm foreground wedge modes are recovered, narrow band dropout redshift uncertainty still precludes a cross-spectrum measurement for the range of survey configurations considered.

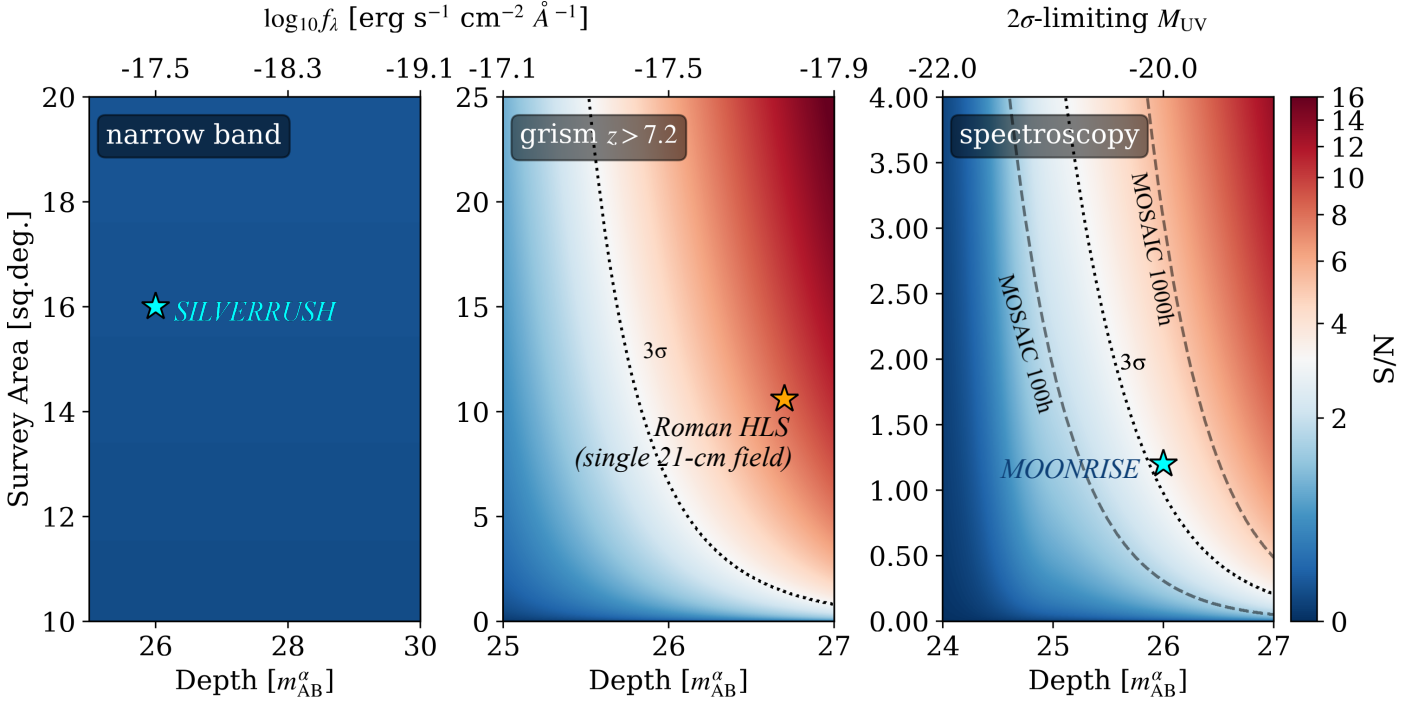


Fig. 8. The effect of observing depth, field of view, and galaxy survey type on the signal-to-noise ratio of a cross-power spectrum detection. Each panel corresponds to a different galaxy survey type, which determines the mean redshift uncertainty associated with that survey. On the top axis of the slit spectroscopy panel we show the corresponding rest frame UV magnitude limit required for $\geq 2\sigma$ completeness of the photometric candidate sample (c.f. Fig. 7). Blue stars correspond to the SILVERRUSH and MOONRISE high-redshift galaxy surveys while the orange star corresponds to an overlap of the Roman HLS survey and a single SKA-low AA* beam; multiple 21-cm fields can be tiled to increase the S/N in quadrature as discussed in the text. We see that the MOONRISE spectroscopic survey should enable a 3σ detection of the cross-spectrum. In the spectroscopy panel we also show 100 and 1000 hour isochrones for potential future surveys using MOSAIC on the ELT.

5.2. HERA–Lyman Alpha

Figure 11 shows our results for a Lyman- α galaxy survey paired with a measurement of the 21-cm signal made using HERA-350. Compared with SKA-low, HERA’s lack of sensitivity to high k_{\perp} modes precludes cross-spectrum detections using galaxy fields with small angular footprints. This is evident in the rightmost panel of Figure 11, where neither MOONRISE nor MOSAIC can yield a cross-spectrum detection with HERA.

The most promising candidate for cross-correlation with HERA are large area surveys with slitless spectroscopy, shown in the middle panel using the benchmark HLS with Roman grism. The star in this panel shows the forecast from La Plante et al. (2023), which we match to within 10%. We predict a $\geq 6\sigma$ detection of the cross-power for a Roman HLS + HERA-350 observation in a single HERA beam covering 100 sq. deg.. Since HERA always operates in drift scan mode, it will observe a cumulative 5 patches of this size in the Roman HLS field, totaling to $S/N = \sqrt{5} \cdot 6 \approx 13.4$ for the full 500 sq. deg. of overlap, very close to the $S/N=14$ quoted by La Plante et al. (2023).

5.3. SKA–OIII/H Alpha

Figure 12 shows our results for a NIRCcam-like galaxy survey targeting H α below $z = 7$ and [OIII]/H β for $z \in (7, 9)$ paired with a 21-cm signal measured by the SKA-low. The bottom two panels show S/N forecasts for cross-correlation using SKA-low AA*, while the top panel uses SKA-low in its planned AA4 upgraded configuration, which includes additional outrigger antennas (Sridhar 2023). The top two panels assume fiducial foregrounds while the bottom panel uses optimistic foregrounds. We

see that fiducial foregrounds preclude detection of the galaxy–21-cm cross-power spectrum a FRESCO-like survey and SKA-low AA*. Even when invoking AA4 or optimistic foregrounds, FRESCO’s footprint remains too small to claim a cross-spectrum detection. This said, a FRESCO-like survey with the same observing depth but 10 \times the survey footprint would yield a $\sim 3\sigma$ detection of the 21-cm signal in cross-correlation using SKA-low AA4. This is not far-fetched since FRESCO itself is only a 53 hour program and produces two non-contiguous pencil beams. Using the same exposure time per pointing, it would only take ~ 240 hours to expand a single FRESCO beam into a field large enough for cross-correlation.

6. Conclusion

A detection of the cosmic 21-cm signal would usher a new era for research on the Epoch of Reionization (EoR). Radio interferometers aim to make a preliminary, low signal-to-noise (S/N) detection of the power spectrum in the coming years. Cross-correlating the preliminary signal with galaxies will provide a crucial sanity check for initial 21-cm detection claims, and potentially enhance the S/N thanks to the tracers’ uncorrelated systematics.

We forecast the S/N of the cross-power in various pairings of prospective galaxy surveys and 21-cm interferometers. Our fiducial 21-cm observations use 1000 hour integrations of the SKA-low AA* and HERA-350. These are paired with galaxy surveys of varying survey area, depth, and selection method (narrow-band, slitless spectroscopy, slit spectroscopy) to compute the galaxy–21-cm cross-power spectrum and quote a S/N for each

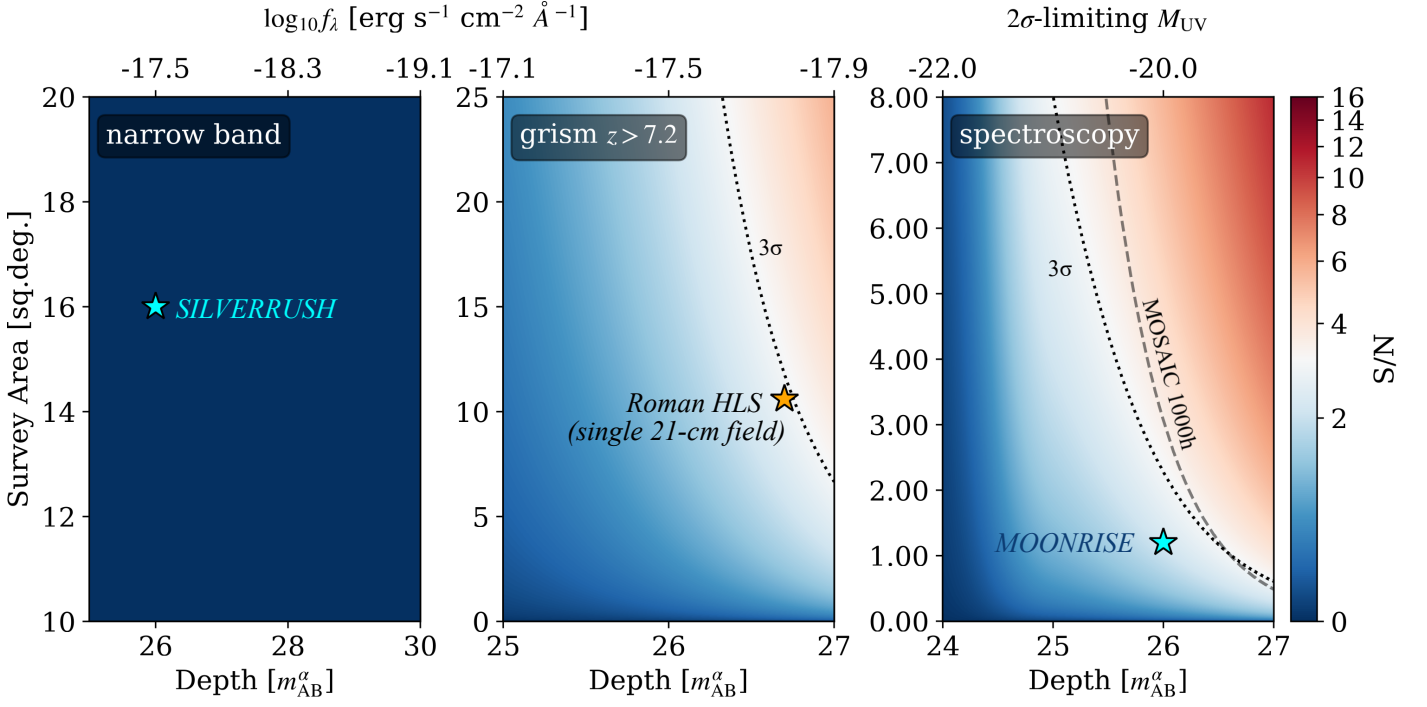


Fig. 9. As Figure 8, but assuming the pessimistic foregrounds shown in Figure 6. Here MOONRISE is no longer sufficient for a 3σ cross-spectrum detection, but a 1000-hour survey with MOSAIC remains viable.

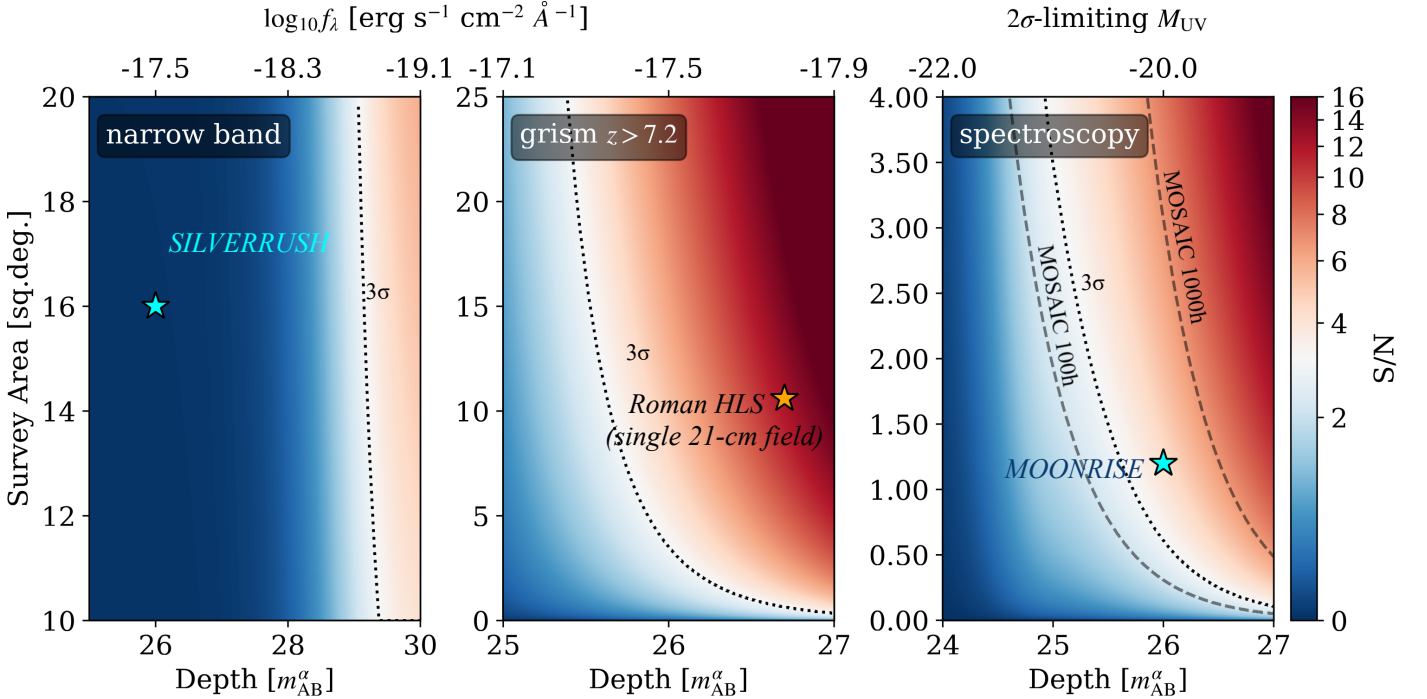


Fig. 10. As Figure 8, but assuming the optimistic foreground scenario in Figure 6. SILVERRUSH remains unviable, although an extremely deep survey of similar angular extent could theoretically breach 3σ , and the S/N with spectroscopy only slightly improves.

scenario. We also vary the level of 21-cm foreground contamination that would be excised before computing the cross-power.

To compute mock observations, we self-consistently simulate large (1 Gpc) galaxy and 21-cm fields using 21cmFASTv4 (Davies et al., in prep). We then post-process the galaxy field to include only galaxies whose line luminosities in a given band (spanning either Lyman- α or H α /H β /OIII) exceeds the sensitivity threshold for the survey of interest. To connect the line lumi-

nosities to a galaxy's continuum magnitude or star formation rate, we sample empirical relations provided by Mason et al. (2018) for Ly- α and Gong et al. (2017) for other lines.

Our mock galaxy surveys are set up for easy comparison with benchmark instruments, including Subaru HyperSupremeCam, Roman grism, VLT MOONS, ELT MOSAIC, and JWST NIR-Cam. Our principal results are:

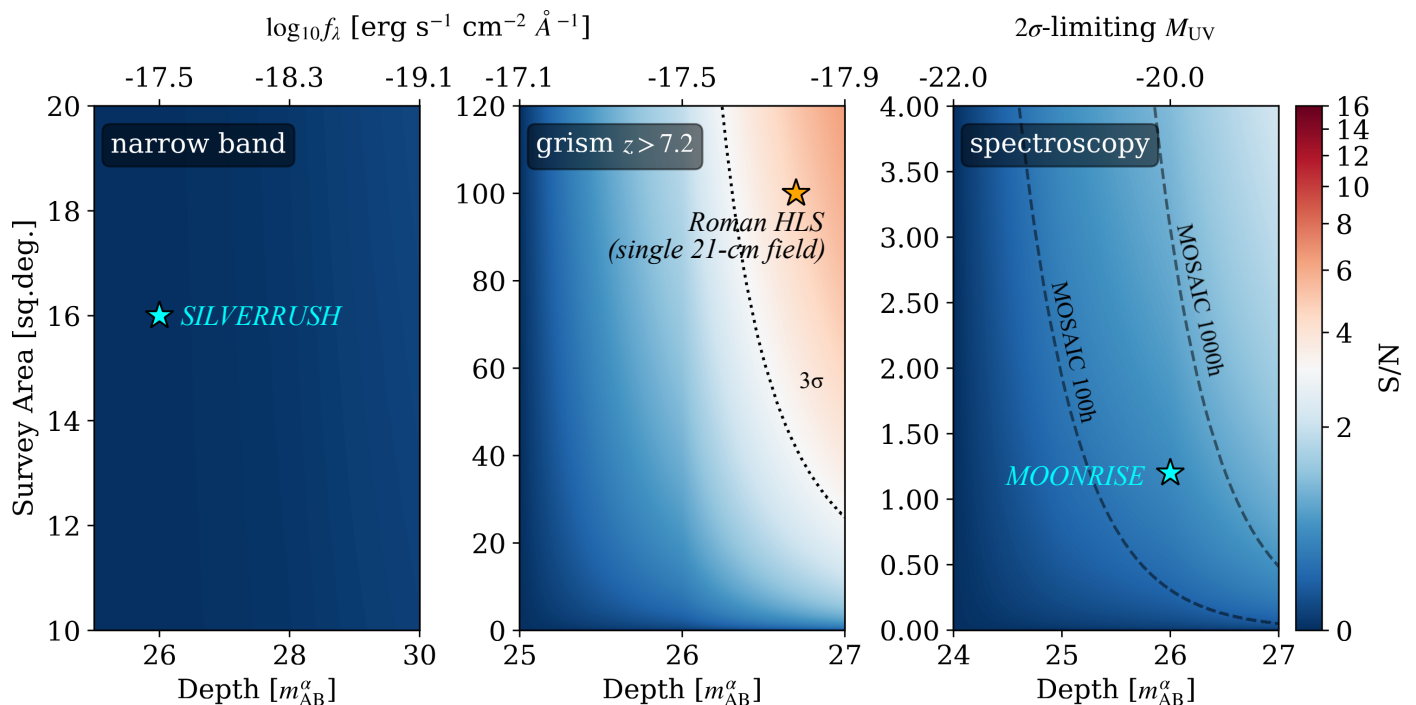


Fig. 11. As Figure 8, but using HERA rather than the SKA-low as the fiducial 21-cm interferometer. Notably, HERA’s lack of sensitivity to high k_{\perp} modes (i.e. small sky plane scales) precludes detection of the cross-spectrum using a galaxy field with a small (~ 5 sq. deg.) field of view. Wide area slitless spectroscopy remains the only viable candidate for cross correlating galaxy maps with HERA 21-cm data.

- Even pessimistic 21-cm foregrounds do not preclude a detection of the cross power with galaxies if the slitless spectroscopic survey area is very large or the slit spectroscopic survey is very deep. Overall, the different foreground contamination scenarios studied here impact the achievable S/N by a factors of few.
- Narrow-band dropout surveys are unlikely to detect the cross-power spectrum due to their poor redshift localization.
- Large-field slitless spectroscopy with Roman grism yields the highest S/N cross-power detection: $\sim 55\sigma$ ($\sim 13\sigma$) paired with SKA-low AA* (HERA-350), for our fiducial model and assuming ~ 500 sq. deg. of overlap. Although the Roman grism is only sensitive to Ly- α at $z \geq 7.2$, Roman’s redshift precision and huge observing area more than makes up for the loss in signal from the missing lower-redshift galaxies.
- Small-field slitless spectroscopy targeting H α /H β OIII using JWST NIRCcam, as per the FRESCO survey (Oesch et al. 2023), does not yield a high enough S/N for a detection of the cross-power spectrum. However, a survey of similar depth which covers ~ 10 times the area would yield a $\sim 3\sigma$ detection of the 21-cm signal in cross-correlation with a 21-cm measurement provided by a planned upgrade of SKA: AA4.
- Slit spectroscopy can provide high S/N cross-power for SKA-low AA* observations. Specifically, the planned MOONRISE survey with VLT MOONS can result in a $\sim 3\sigma$ detection (Maiolino et al. 2020). We likewise show that a 4σ detection can be made with ELT MOAIC for a comparable observation time, for a survey with area ~ 1 – 3 sq. deg. (Evans et al. 2015).

These forecasts are intended as a guide for future survey strategies, facilitating the detection of the galaxy–21-cm cross-power spectrum.

Acknowledgements. We thank S. Murray for helpful guidance regarding the generation of noise for the 21-cm field. Additional thanks to D. Breitman for pro-

viding a handy script for rapid power spectrum calculations. We extend further gratitude to S. Carniani, L. Pentericci, and M. Hayes for useful discussions regarding upcoming surveys, as well as to A. C. Liu for invaluable feedback on a draft version of this paper. We gratefully acknowledge computational resources of the HPC center at SNS. AM acknowledges support from the Italian Ministry of Universities and Research (MUR) through the PRIN project "Optimal inference from radio images of the epoch of reionization", and the PNRR project "Centro Nazionale di Ricerca in High Performance Computing, Big Data e Quantum Computing".

References

- Adachi, S., Adkins, T., Aguilar Faúndez, M. A. O., et al. 2022, *ApJ*, 931, 101
 Adi, T., Flitter, J., & Kovetz, E. D. 2024, arXiv e-prints, arXiv:2410.22424
 Anderson, C. J., Luciw, N. J., Li, Y. C., et al. 2018, *MNRAS*, 476, 3382
 Barrow, K. S. S., Wise, J. H., Norman, M. L., O’Shea, B. W., & Xu, H. 2017, *MNRAS*, 469, 4863
 Berkhout, L. M., Jacobs, D. C., Abdurashidova, Z., et al. 2024, *PASP*, 136, 045002
 Bianco, M., Giri, S. K., Prelogović, D., et al. 2024, *MNRAS*, 528, 5212
 Bird, S., Ni, Y., Di Matteo, T., et al. 2022, *MNRAS*, 512, 3703
 Bouwens, R. J., Illingworth, G. D., Oesch, P. A., et al. 2015, *ApJ*, 811, 140
 Bouwens, R. J., Illingworth, G. D., Oesch, P. A., et al. 2014, *The Astrophysical Journal*, 793, 115
 Bouwens, R. J., Oesch, P. A., Stefanon, M., et al. 2021, *AJ*, 162, 47
 Ceverino, D., Klessen, R. S., & Glover, S. C. O. 2018, *MNRAS*, 480, 4842
 Chakraborty, A. & Choudhury, T. R. 2024, *J. Cosmology Astropart. Phys.*, 2024, 078
 CHIME Collaboration, Amiri, M., Bandura, K., et al. 2023a, arXiv e-prints, arXiv:2309.04404
 CHIME Collaboration, Amiri, M., Bandura, K., et al. 2023b, *ApJ*, 947, 16
 Clark, S. J., Dutta, B., Gao, Y., Ma, Y.-Z., & Strigari, L. E. 2018, *Phys. Rev. D*, 98, 043006
 Cooray, A., Bock, J., Burgarella, D., et al. 2016, arXiv e-prints, arXiv:1602.05178
 Crites, A. T., Bock, J. J., Bradford, C. M., et al. 2014, in *Society of Photo-Optical Instrumentation Engineers (SPIE) Conference Series*, Vol. 9153, Millimeter, Submillimeter, and Far-Infrared Detectors and Instrumentation for Astronomy VII, ed. W. S. Holland & J. Zmuidzinas, 91531W
 Cunnington, S., Li, Y., Santos, M. G., et al. 2023, *MNRAS*, 518, 6262
 Curti, M., Mannucci, F., Cresci, G., & Maiolino, R. 2020, *MNRAS*, 491, 944

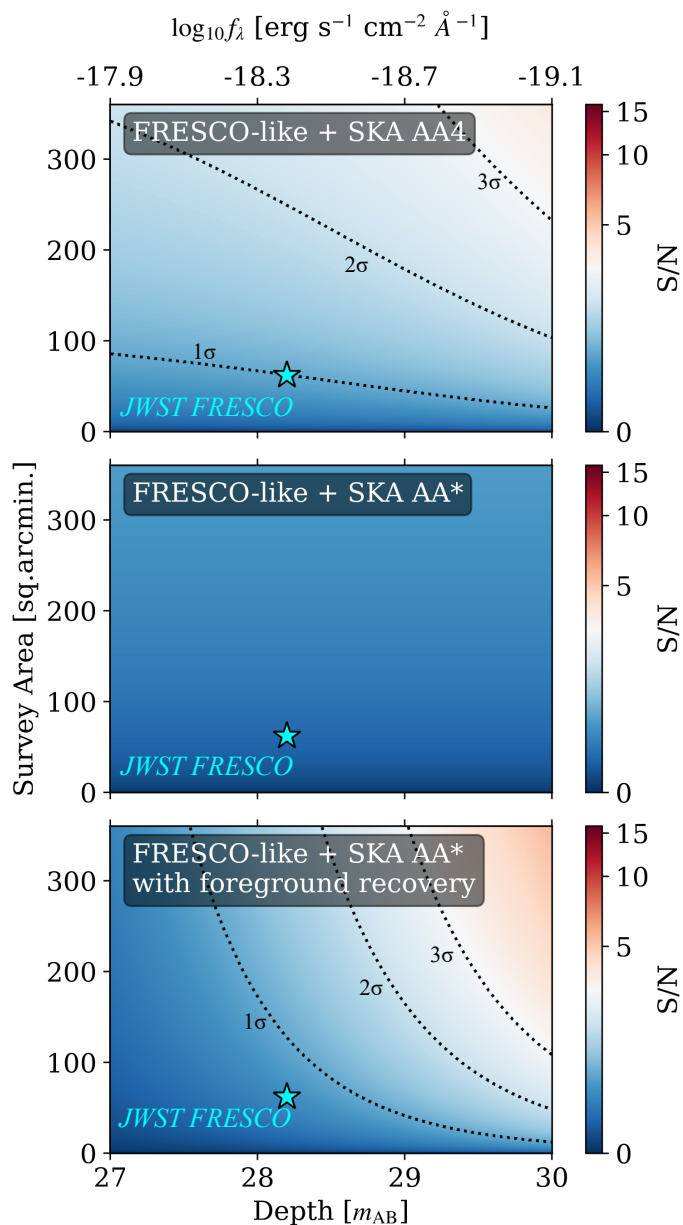


Fig. 12. The effect of observing depth and field of view on a FRESKO-like survey which selects for $H\alpha$ at $z < 7$ and $[OIII]/H\beta$ at $z \geq 7$. FRESKO's 62 square arcminute fields are too small to yield a detection of the 21-cm cross-power spectrum.

Datta, A., Bowman, J. D., & Carilli, C. L. 2010, *The Astrophysical Journal*, 724, 526–538
 Davies, J. E. in prep.
 Davies, J. E., Bird, S., Mutch, S., et al. 2023, *MNRAS*, 525, 2553
 De Barros, S., Pentericci, L., Vanzella, E., et al. 2017, *A&A*, 608, A123
 Dillon, J. S., Liu, A., Williams, C. L., et al. 2014, *Physical Review D*, 89
 Euclid Collaboration, McPartland, C. J. R., Zalesky, L., et al. 2024, arXiv e-prints, arXiv:2408.05275
 Evans, C., Puech, M., Afonso, J., et al. 2015, arXiv e-prints, arXiv:1501.04726
 Facchinetti, G., Lopez-Honorez, L., Qin, Y., & Mesinger, A. 2024, *J. Cosmology Astropart. Phys.*, 2024, 005
 Feldman, H. A., Kaiser, N., & Peacock, J. A. 1994, *ApJ*, 426, 23
 Finkelstein, S. L., Ryan, Russell E. J., Papovich, C., et al. 2015, *ApJ*, 810, 71
 Fisher, K. B., Davis, M., Strauss, M. A., Yahil, A., & Huchra, J. P. 1993, *ApJ*, 402, 42
 Fragos, T., Lehmer, B. D., Naoz, S., Zezas, A., & Basu-Zych, A. 2013, *ApJ*, 776, L31
 Fronenberg, H. & Liu, A. 2024, *ApJ*, 975, 222
 Furlanetto, S. R. & Lidz, A. 2007, *ApJ*, 660, 1030
 Furlanetto, S. R., Zaldarriaga, M., & Hernquist, L. 2004, *ApJ*, 613, 1

Gagnon-Hartman, S., Cui, Y., Liu, A., & Ravanbakhsh, S. 2021, *MNRAS*, 504, 4716
 Gillet, N. J. F., Mesinger, A., & Park, J. 2020, *MNRAS*, 491, 1980
 Gong, Y., Cooray, A., Silva, M. B., et al. 2017, *ApJ*, 835, 273
 Grazian, A., Giallongo, E., Paris, D., et al. 2017, *A&A*, 602, A18
 Gunn, J. E. & Peterson, B. A. 1965, *ApJ*, 142, 1633
 Heneka, C. & Cooray, A. 2021, *MNRAS*, 506, 1573
 Heneka, C. & Mesinger, A. 2020, *MNRAS*, 496, 581
 Hothi, I., Chapman, E., Pritchard, J. R., et al. 2020, *Monthly Notices of the Royal Astronomical Society*, 500, 2264–2277
 Hutter, A., Dayal, P., Müller, V., & Trott, C. M. 2017, *ApJ*, 836, 176
 Hutter, A., Heneka, C., Dayal, P., et al. 2023, *MNRAS*, 525, 1664
 Hutter, A., Trott, C. M., & Dayal, P. 2018, *MNRAS*, 479, L129
 Izotov, Y. I., Schaerer, D., Thuan, T. X., et al. 2016, *MNRAS*, 461, 3683
 Kennedy, J., Carr, J. C., Gagnon-Hartman, S., et al. 2024, *MNRAS*, 529, 3684
 Kennicutt, Robert C., J. 1998, *ARA&A*, 36, 189
 Kern, N. S., Parsons, A. R., Dillon, J. S., et al. 2020, *ApJ*, 888, 70
 Kimm, T., Cen, R., Devriendt, J., Dubois, Y., & Slyz, A. 2015, *MNRAS*, 451, 2900
 Kostyuk, I., Ciardi, B., & Ferrara, A. 2023, arXiv e-prints, arXiv:2308.01476
 Kovetz, E. D., Viero, M. P., Lidz, A., et al. 2017, arXiv e-prints, arXiv:1709.09066
 Kubota, K., Inoue, A. K., Hasegawa, K., & Takahashi, K. 2020, *MNRAS*, 494, 3131
 Kubota, K., Yoshiura, S., Takahashi, K., et al. 2018, *MNRAS*, 479, 2754
 La Plante, P., Mirocha, J., Gorce, A., Lidz, A., & Parsons, A. 2023, *ApJ*, 944, 59
 La Plante, P., Sippl, J., & Lidz, A. 2022, *ApJ*, 928, 162
 Lehmer, B. D., Eufrazio, R. T., Tzanavaris, P., et al. 2019, *ApJS*, 243, 3
 Lidz, A., Zahn, O., Furlanetto, S. R., et al. 2009, *ApJ*, 690, 252
 Liu, A., Parsons, A. R., & Trott, C. M. 2014a, *Phys. Rev. D*, 90, 023018
 Liu, A., Parsons, A. R., & Trott, C. M. 2014b, *Phys. Rev. D*, 90, 023019
 Liu, A. & Shaw, J. R. 2020, *PASP*, 132, 062001
 Ly, C., Malkan, M. A., Kashikawa, N., et al. 2007, *ApJ*, 657, 738
 Ma, Q., Helgason, K., Komatsu, E., Ciardi, B., & Ferrara, A. 2018, *MNRAS*, 476, 4025
 Maiolino, R., Cirasuolo, M., Afonso, J., et al. 2020, *The Messenger*, 180, 24
 Mao, X.-C. 2014, *ApJ*, 790, 148
 Mason, C. A., Treu, T., Dijkstra, M., et al. 2018, *ApJ*, 856, 2
 Masui, K. W., Switzer, E. R., Banavar, N., et al. 2013, *ApJ*, 763, L20
 Mesinger, A. & Furlanetto, S. 2007, *ApJ*, 669, 663
 Mesinger, A., Furlanetto, S., & Cen, R. 2011, *MNRAS*, 411, 955
 Mesinger, A. & Furlanetto, S. R. 2008, *MNRAS*, 386, 1990
 Miralda-Escudé, J. 1998, *ApJ*, 501, 15
 Mirocha, J. & Furlanetto, S. R. 2019, *MNRAS*, 483, 1980
 Mirocha, J., Furlanetto, S. R., & Sun, G. 2017, *MNRAS*, 464, 1365
 Moriwaki, K., Beane, A., & Lidz, A. 2024, *MNRAS*, 530, 3183
 Moriwaki, K. & Yoshida, N. 2021, *ApJ*, 923, L7
 Munshi, S., Mertens, F. G., Koopmans, L. V. E., et al. 2025, *A&A*, 693, A276
 Murray, S., Pober, J., & Kolopanis, M. 2024, *The Journal of Open Source Software*, 9, 6501
 Nikolić, I., Mesinger, A., Greig, B., & Gillet, N. 2024, *MNRAS*, 484, 933
 Nikolić, I., Mesinger, A., Qin, Y., & Gorce, A. 2023, *MNRAS*, 526, 3170
 Oesch, P. A., Brammer, G., Naidu, R. P., et al. 2023, *MNRAS*, 525, 2864
 Oke, J. B. & Gunn, J. E. 1983, *ApJ*, 266, 713
 Ouchi, M., Harikane, Y., Shibuya, T., et al. 2018, *PASJ*, 70, S13
 Oyarzún, G. A., Blanc, G. A., González, V., Mateo, M., & Bailey, John I., I. 2017, *ApJ*, 843, 133
 Pacucci, F., Mesinger, A., Mineo, S., & Ferrara, A. 2014, *MNRAS*, 443, 678
 Pahl, A. J., Shapley, A., Steidel, C. C., et al. 2023, *MNRAS*, 521, 3247
 Pallottini, A. & Ferrara, A. 2023, *A&A*, 677, L4
 Park, J., Mesinger, A., Greig, B., & Gillet, N. 2019, *MNRAS*, 484, 933
 Parshley, S. C., Kronshage, J., Blair, J., et al. 2018, in *Society of Photo-Optical Instrumentation Engineers (SPIE) Conference Series*, Vol. 10700, Ground-based and Airborne Telescopes VII, ed. H. K. Marshall & J. Spyromilio, 107005X
 Pober, J. C. 2014, *Monthly Notices of the Royal Astronomical Society*, 447, 1705–1712
 Pober, J. C., Liu, A., Dillon, J. S., et al. 2014, *The Astrophysical Journal*, 782, 66
 Prelogović, D. & Mesinger, A. 2023, *MNRAS*, 524, 4239
 Qin, Y., Mesinger, A., Prelogović, D., et al. 2024, arXiv e-prints, arXiv:2412.00799
 Rath, E., Pascua, R., Josaitis, A. T., et al. 2024, arXiv e-prints, arXiv:2406.08549
 Reichardt, C. L., Patil, S., Ade, P. A. R., et al. 2021, *ApJ*, 908, 199
 Seo, H.-J. & Eisenstein, D. J. 2003, *ApJ*, 598, 720
 Sobacchi, E., Mesinger, A., & Greig, B. 2016, *MNRAS*, 459, 2741
 Sridhar, S. 2023, SKAO staged delivery, array assemblies and layouts, Technical report SKAO-TEL-0002299, SKAO
 Steidel, C. C., Bogosavljević, M., Shapley, A. E., et al. 2018, *ApJ*, 869, 123
 Sun, G. & Furlanetto, S. R. 2016, *MNRAS*, 460, 417
 Talia, M., Schreiber, C., Garilli, B., et al. 2023, *A&A*, 678, A25
 Thyagarajan, N., Jacobs, D. C., Bowman, J. D., et al. 2015, *ApJ*, 807, L28
 Umeda, H., Ouchi, M., Kikuta, S., et al. 2024, arXiv e-prints, arXiv:2411.15495
 Villanueva-Domingo, P. 2021, arXiv e-prints, arXiv:2112.08201
 Vrbanc, D., Ciardi, B., Jelić, V., et al. 2020, *MNRAS*, 492, 4952
 Wang, Y., Zhai, Z., Alavi, A., et al. 2022, *ApJ*, 928, 1
 Xu, D., Springel, V., Sluse, D., et al. 2017, *MNRAS*, 469, 1824
 Yang, S., Popping, G., Somerville, R. S., et al. 2022, *ApJ*, 929, 140

Appendix A: IGM Optical Depth to Lyman-alpha

The above relations for computing Ly- α luminosity from M_{UV} were calibrated against observation from redshifts 3–4.6, a time when the IGM was already ionized, meaning that while they include the effects of attenuation from HI in the ISM/CGM, they do not include any attenuation from the IGM (Oyarzún et al. 2017). To account for the optical depth of the IGM at our redshifts of interest, we adapted the model of Mesinger & Furlanetto (2008), which provided analytic relations for the IGM attenuation of rest-wavelength Ly- α emission for halos of a given mass and mean ionization fraction at $z = 9$. We opted to use this analytic relation for simplicity's sake, deferring a realistic treatment of Ly- α attenuation along sightlines in the IGM to a future work. Mesinger & Furlanetto (2008) found that the distribution of IGM optical depths for a halo of a given mass in a region of given mean neutral fraction is well-described by the log-normal distribution

$$\frac{\partial p(> \tau_{\text{IGM},9})}{\partial \tau_{\text{IGM},9}} = \frac{1}{\tau_{\text{IGM},9} \sqrt{2\pi\sigma_{\text{IGM},9}^2}} \exp\left[-\frac{(\ln \tau_{\text{IGM},9} - \mu_{\text{IGM},9})^2}{2\sigma_{\text{IGM},9}^2}\right], \quad (\text{A.1})$$

where

$$\mu_{\text{IGM},9} = -3.37 + \log_{10} M_{10}(-0.115 - 0.587\bar{x}_{\text{HI}}) + 5.30\bar{x}_{\text{HI}}, \quad (\text{A.2})$$

$$\sigma_{\text{IGM},9} = 1.68 + \log_{10} M_{10}(-0.115 - 0.285\bar{x}_{\text{HI}}) - 1.08\bar{x}_{\text{HI}}, \quad (\text{A.3})$$

wherein $M_h = M_{10} \cdot 10^{10} M_{\odot}$ is the halo mass and \bar{x}_{HI} is the mean neutral fraction of the IGM surrounding the halo.

We extend this model in two ways, firstly by generalizing to other redshifts, and secondly by accounting for the frequency-dependence of the IGM optical depth. We account for the first effect simply by scaling the optical depth with the mean density of the Universe, i.e.,

$$\tau_{\text{EoR}}(z) = \tau_{\text{IGM},9} \left(\frac{1+z}{10}\right)^3. \quad (\text{A.4})$$

For the latter effect, we use the Miralda-Escudé equation for the Ly- α damping wing and normalize it such that its value at rest wavelength equals the value provided by Mesinger & Furlanetto (2008) (Miralda-Escudé 1998). The Miralda-Escudé equation is

$$\tau_{\text{ME}}(z) = \tau_{\text{GP}} \frac{R_{\alpha}}{\pi} \left(\frac{1+z_b}{1+z}\right)^{1.5} \left[I\left(\frac{1+z_b}{1+z}\right) - I\left(\frac{1+z_e}{1+z}\right) \right], \quad (\text{A.5})$$

where $\tau_{\text{GP}} = 7.16 \cdot 10^5 ((1+z)/10)^{1.5}$ is the Gunn-Peterson optical depth (Gunn & Peterson 1965), $R_{\alpha} = 6.25 \cdot 10^8 / (4\pi\nu_{\text{Ly}\alpha})$ is the decay scale of Ly- α emission, wherein $\nu_{\text{Ly}\alpha}$ is the frequency of Ly- α emission, $z = (\lambda/\lambda_{\text{Ly}\alpha})(1+z_s) - 1$ is the redshift corresponding to a rest wavelength λ , wherein $\lambda_{\text{Ly}\alpha}$ is the rest wavelength of the Ly- α line, z_s is the systemic redshift of the LAE, z_b is the redshift whereat the Ly- α emission first interacts with the neutral IGM, taken in this study to be $z_b = z_s - 0.02$, z_e is the redshift whereat the Ly- α emission exits the neutral IGM, taken to be $z_e = 5.5$, and finally

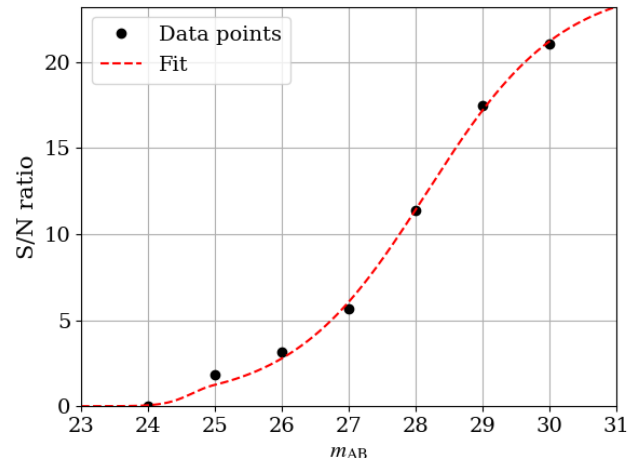


Fig. B.1. The fit function for the signal-to-noise ratio as a function of observing depth for a spectroscopic survey with a field of view of 1 square degree.

$$I(x) \equiv \frac{x^{9/2}}{1-x} + \frac{9}{7}x^{7/2} + \frac{9}{5}x^{5/2} + 3x^{3/2} + 9x^{1/2} - \ln \left| \frac{1+x^{1/2}}{1-x^{1/2}} \right| \quad (\text{A.6})$$

accounts for the shape of the Ly- α transmission curve.

Combining all parts, our equation for the Ly- α optical depth as a function of rest-frame wavelength and systemic redshift is

$$\tau_{\text{EoR}}(\lambda) = \tau_{\text{IGM},9} \frac{\tau_{\text{ME}}(\lambda)}{\tau_{\text{ME}}(z_s)} \left(\frac{1+z_s}{10}\right)^3. \quad (\text{A.7})$$

Appendix B: Signal-to-Noise Ratio as a Function of Observing Depth

We produce each panel of Figures 8, 9, and 10 using only three realizations of the biased galaxy field. For both galaxy selection criteria, we generate mock observations with m_{AB} sensitivities of 25, 26, 27, 28, 29, and 30. In order to produce a S/N gradient across the full range of magnitudes in each panel, we require a means of interpolating the S/N between each realization.

We adopt a double sigmoid function of the form

$$\frac{S}{N}(m_{\text{AB}}) = \begin{cases} h_1(1 + \exp\{-k_1(m_{\text{AB}} - r_1)\})^{-1} & m_{\text{AB}} \leq 25 \\ h_2(1 + \exp\{-k_2(m_{\text{AB}} - r_2)\})^{-1} & m_{\text{AB}} > 25 \end{cases}$$

We chose this form since it obeys the limit of approaching zero as the limiting magnitude approaches zero (the limit where no galaxies are detected) as well as the limit wherein it approaches some maximum S/N as the limiting magnitude tends to infinity (the limit where all galaxies are detected). We chose to use a double sigmoid rather than a typical sigmoid since it tends to fit the data better. Figure B.1 illustrates $\frac{S}{N}(m_{\text{AB}}|\delta_z)$ for a spectroscopic Ly- α survey assuming normal 21-cm foregrounds and a field of view of 1 square degree.

Appendix C: Increasing Field of View versus Observing Depth

The S/N in the cross-power spectrum increases when either the field of view of the galaxy survey or its limiting magnitude increases, as seen in Figures 8-12. In designing a galaxy survey

for the purpose of cross-correlation with the 21-cm signal, one asks: what is the better use of observing time? Increasing the total number of telescope pointings or increasing the integration time per pointing?

Let us proceed with a very basic mathematical argument for favoring the field of view over the observing depth. Consider a survey of variable total observing time, t . The field of view of the survey scales linearly with t ,

$$\text{FoV} \propto t. \quad (\text{C.1})$$

Meanwhile the observing depth (in magnitudes) scales logarithmically with t via

$$m_{\text{AB}} \propto \ln(t). \quad (\text{C.2})$$

From Equation 27 we know that for a fixed observing depth the S/N in the detection of the cross-power spectrum scales as the square root of the field of view, i.e.,

$$\hat{s}_{\text{fixed depth}} \propto \text{FoV}^{1/2} \propto t^{1/2}. \quad (\text{C.3})$$

For direct comparison, let us produce an analogous scaling relation for S/N with a fixed field of view and varying observing depth. In Appendix B we produced a functional form for the dependence of S/N on observing depth by fitting a double sigmoid to the results of our forward model. Here let us consider only the upper sigmoid, which is a simple sigmoid limited to the domain $m_{\text{AB}} \geq 25$. Here,

$$\hat{s}_{\text{fixed FoV}} = h[1 + \exp\{-k(m_{\text{AB}} - r)\}]^{-1} + c. \quad (\text{C.4})$$

Letting $m_{\text{AB}} = C \ln(t) + D$ and substituting this into the above equation, we obtain

$$\hat{s}_{\text{fixed FoV}} = h[1 + t^{-kC} e^{kr-kD}]^{-1} + c. \quad (\text{C.5})$$

To evaluate whether increasing observing depth for fixed field of view or vice versa is a more efficient use of observing time, let us evaluate the ratio $\hat{s}'_{\text{fixed FoV}}/\hat{s}'_{\text{fixed depth}}$, where ' indicates a partial derivative with respect to time. For a survey of fixed observing depth, the S/N scales via

$$\hat{s}_{\text{fixed depth}} = \frac{\hat{s}_0}{t_0^{1/2}} t^{1/2}, \quad (\text{C.6})$$

where \hat{s}_0 is the S/N of some reference survey using the same instrument and t_0 is the time required to produce that survey. The partial derivative of this equation with respect to time is

$$\hat{s}'_{\text{fixed depth}} = \frac{\hat{s}_0}{t_0^{1/2} t^{1/2}}. \quad (\text{C.7})$$

Now let us take the partial derivative of $\hat{s}_{\text{fixed FoV}}$ to produce

$$\hat{s}'_{\text{fixed FoV}} = hkC e^{kr-kD} t^{-kC} [1 + t^{-kC} e^{kr-kD}]^{-2}. \quad (\text{C.8})$$

Therefore, the ratio of these quantities is

$$\mathcal{R} \equiv \frac{\hat{s}'_{\text{fixed FoV}}}{\hat{s}'_{\text{fixed depth}}} = \frac{t_0^{1/2}}{\hat{s}_0} hkC e^{kr-kD} t^{-kC-1/2} [1 + t^{-kC} e^{kr-kD}]^{-2}. \quad (\text{C.9})$$

Now let us simplify the above expression by defining $\alpha = \frac{t_0^{1/2}}{\hat{s}_0} h$, $\beta = e^{kr-kD}$, and $\gamma = kC$, allowing us to write

$$\mathcal{R} = \alpha\beta\gamma t^{-\gamma-1/2} [1 + \beta t^{-\gamma}]^{-2}. \quad (\text{C.10})$$

If γ is positive, then \mathcal{R} is positive and defined only for $t > 0$ and has one critical point, a maximum. Recall that if $\mathcal{R} > 1$, then increasing observing depth for a fixed field of view is more efficient than increasing field of view for a fixed observing depth; if $\mathcal{R} < 1$, then the reverse is true. A simple way to see whether the former is *ever* true is to check whether the maximum value of \mathcal{R} is greater than 1.

When we vary either the field of view or the observing depth, we vary them with respect to some fixed configuration of field of view, depth, t_0 , and \hat{s}_0 . This necessarily requires some assumptions about the survey configuration, including the instrument's limiting magnitude, field of view per pointing, galaxy selection criterion, 21-cm instrument, and 21-cm foregrounds. In what follows, let us consider perturbations of a spectroscopic survey which uses Lyman- α -selected galaxies and is paired with a 21-cm measurement from the SKA (i.e., the experiment shown in the rightmost panel of Figure 8). The fixed point in our analysis shall consist of a survey covering 1 square degree at a depth of $m_{\text{AB}} = 26$. Such a survey yields a S/N of $\hat{s}_0 = 2.78$. The amount of time required to complete a survey depends on its telescope's field of view per pointing, A_I , and 5-hour 5σ limiting magnitude, $m_{\text{AB},0}$ via the relation

$$t = \frac{1}{A_I} 10^{\frac{4}{5}(m_{\text{AB}} - m_{\text{AB},0})}, \quad (\text{C.11})$$

which for $m_{\text{AB}} = 26$ yields $t_0 = A_I^{-1} 10^{4(26 - m_{\text{AB},0})/5}$.

Having determined our reference survey, let us now find the critical point of \mathcal{R} . The partial derivative of \mathcal{R} with respect to t is

$$\mathcal{R}' = -\alpha\beta\gamma t^{-\gamma-3/2} [1 + \beta t^{-\gamma}]^{-2} \times \left\{ \left(\gamma + \frac{1}{2} \right) - 2\beta\gamma t^{-\gamma} [1 + \beta t^{-\gamma}]^{-1} \right\}. \quad (\text{C.12})$$

The maximum occurs when $\mathcal{R}' = 0$, and solving the above yields a critical time of

$$t_c = \left[\frac{1}{\beta} \left(\frac{2\beta\gamma}{\gamma + \frac{1}{2}} - 1 \right) \right]^{-1/\gamma}. \quad (\text{C.13})$$

Substitution into the equation for \mathcal{R} reveals a maximum value of

$$\mathcal{R}_{\text{max}} = \frac{\alpha}{4\beta\gamma} \left(\gamma + \frac{1}{2} \right)^2 \left[\frac{1}{\beta} \left(\frac{2\beta\gamma}{\gamma + \frac{1}{2}} - 1 \right) \right]^{1+2/\gamma}. \quad (\text{C.14})$$

Now let us evaluate the above for realistic values of α , β , and γ . α depends on t_0 , \hat{s}_0 , and h . t_0 depends on the field of view and limiting magnitude of the specific instrument used for the survey while \hat{s}_0 and h are fixed by the redshift uncertainty,

galaxy selection criterion, 21-cm instrument, and 21-cm foregrounds assumed in the model. For our SKA-spectroscopic survey example, $\hat{s} = 2.78$ and $h = 24.34$, giving us

$$\alpha = 8.75A_I^{-1/2}10^{2(26-m_{AB,0})/5}. \quad (\text{C.15})$$

Next we have β , which depends on k , r , and D . $k = 0.99$ and $r = 28.17$ are fixed by the same criteria as h whereas D depends on our choice of instrument. Rearranging Equation C.11 yields

$$m_{AB} = \frac{5}{4 \ln 10} \ln t + \frac{5}{4 \ln 10} \ln A_I + m_{AB,0}, \quad (\text{C.16})$$

wherein $D = \frac{5}{4 \ln 10} \ln A_I + m_{AB,0}$ and $C = \frac{5}{4 \ln 10}$ with reference to our aforementioned form for $m_{AB}(t)$. Therefore,

$$\beta = A_I^{-0.54} \exp\{0.99(29.17 - m_{AB,0})\}. \quad (\text{C.17})$$

Finally,

$$\gamma = 0.54. \quad (\text{C.18})$$

Substituting these relations into the equation for \mathcal{R}_{\max} yields

$$\mathcal{R}_{\max} = 2.32A_I^{0.03} \cdot 10^{2(26-m_{AB,0})/5} e^{0.99(m_{AB,0}-28.17)} \times [1.03A_I^{0.03} - A_I^{0.53} e^{0.99(m_{AB,0}-28.17)}]^{4.77}. \quad (\text{C.19})$$

Now we have an equation which depends only on the field of view per pointing and limiting magnitude of an instrument. Varying these allows us to explore various possible spectroscopic survey instruments, as long as they select for Lyman- α emission and are cross-correlated with a 21-cm detection made using SKA-low.

Figure C.1 summarizes the results of our investigation. We find that for all values of $A_I \in (25, 1000)$ square arcminutes and $m_{AB,0} \in (25, 28)$, it is more time-efficient to increase the field of view of the survey rather than increasing its depth, relative to a fiducial survey which covers 1 square degree with a depth of $m_{AB} = 26$. Therefore, we say that for any realistic spectroscopic survey, the optimal survey design for the purposes of maximizing the signal in the cross-power spectrum is to target a depth of $m_{AB} \sim 26$ and cover as much contiguous area on the sky as possible.

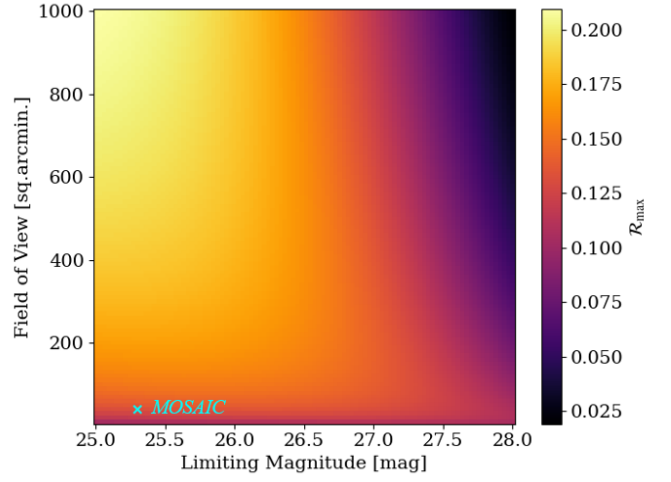


Fig. C.1. The maximum value of the ratio between the signal gain per unit observing time for fixed field of view to the same for fixed observing depth, calculated for various telescope fields of view and limiting magnitudes. All values are calculated with reference to a Lyman- α -selected galaxy survey with spectroscopic redshifts used for cross-correlation with a 21-cm measurement from SKA-low, assuming that 21-cm foregrounds extend to the horizon. Values greater than one would indicate that increasing the observing depth yields more signal than increasing the field of view, for the same amount of time spent. All values in the domain shown are less than one, indicating that increasing the field of view yields more signal per unit time than increasing the observing depth.